Improved modeling of photon observables with the event-by-event fission model FREYA

R. Vogt[1,2] and J. Randrup[3]
[1]*Nuclear and Chemical Sciences Division, Lawrence Livermore National Laboratory, Livermore, California 94551, USA*
[2]*Physics Department, University of California, Davis, California 95616, USA*
[3]*Nuclear Science Division, Lawrence Berkeley National Laboratory, Berkeley, California 94720, USA*
(Received 23 August 2017; published 28 December 2017)

The event-by-event fission model FREYA has been improved, in particular to address deficiencies in the calculation of photon observables. We discuss the improvements that have been made and introduce several new variables, some detector dependent, that affect the photon observables. We show the sensitivity of FREYA to these variables. We then compare the results to the available photon data from spontaneous and thermal neutron-induced fission.

DOI: 10.1103/PhysRevC.96.064620

I. INTRODUCTION

The computational model FREYA generates complete fission events, i.e., it provides the full kinematic information on the two product nuclei as well as all the emitted neutrons and photons. In its development, an emphasis had been put on speed, so large event samples can be generated quickly. FREYA therefore relies on experimental data supplemented by simple physics-based modeling.

In its standard version, to treat a given fission case, FREYA needs the fission fragment mass distribution, $Y(A)$, and the average total kinetic energy for each mass split, TKE(A), for the particular excitation energy considered. $Y(A)$ is taken either directly as the measured yields or as a five-Gaussian fit to the data which makes it possible to parametrize its energy dependence; see Ref. [1] for details on how the energy dependence of neutron-induced fission is handled in FREYA.

In order to generate an event, FREYA selects the mass split based on the provided $Y(A)$. The fragment charges are then sampled from the normal distributions suggested by experiment [1]. The linear and angular momenta of the two fragments and their internal excitations are subsequently sampled. After their formation, the fully accelerated fragments de-excite first by neutron evaporation and then by photon emission. In addition to spontaneous fission, FREYA treats neutron-induced fission up to $E_n = 20$ MeV. The possibility of prefission evaporation is considered as well as pre-equilibrium neutron emission. Both play an increasing role at the higher energies.

This paper is a followup to our previous paper on prompt photon emission from fission [2], describing several improvements to the modeling of photon emission. For detailed information on how to download and run FREYA, the first published fission event generator, see Ref. [3] and the subsequent new version announcement that includes the new work described here [4].

This paper is organized as follows. We first discuss the improvements made to the photon model in FREYA. We then describe the model parameters of FREYA and which observables they affect most strongly. We then show how the improvements affect prompt photon observables. Next, we demonstrate the effect of modifying the FREYA parameters on the photon results, in particular for ^{252}Cf(sf) because a first attempt at fitting the FREYA parameters to data with this version of FREYA was made for this case [5].

We then compare our results to photon data from ^{252}Cf(sf) as well as from neutron-induced fission when appropriate. Because no detailed fits have been made for those cases, the parameter that governs photon emission has the value determined in a global fit to available ^{252}Cf(sf) data [5], as explained further in the text. The calculations for those cases then yield a reasonable preliminary result. Finally we conclude.

II. FREYA

General descriptions of the physics of FREYA have been published elsewhere [1,2,6–8]. Therefore, in this paper we describe only the improvements made for photon emission.

In our previous paper on photon emission [2], we included statistical emission of photons with no form factor modulation, corresponding to black-body radiation. The resulting photon spectrum was too soft, with too few high-energy photons. In addition, although rotational energy was included, the total angular momentum was not conserved. Furthermore, the earlier treatment did not include any discrete low-energy photon transitions, but carried the statistical de-excitation through until the yrast line was reached and then disposed of the remaining rotational energy by schematic $E2$ transitions (the magnitude of the angular momentum S_f was reduced by 2 and the emitted photon carried off the corresponding difference in the rotational energy $S_\mathrm{f}^2/2\mathcal{I}_\mathrm{f}$) [2].

For each fragment, the *initial* magnitude of its angular momentum was governed by a "spin temperature" T_S, $\langle S_\mathrm{f}^2\rangle = 2\mathcal{I}_\mathrm{f} T_S$, where $\mathcal{I}_\mathrm{f}$ is the fragment moment of inertia (which is generally taken as 0.3 times the rigid value). The parameter T_S was varied from 0.35 to 2.75 MeV for a fixed value of Q_min, the energy above the neutron separation energy at which the fragment de-excitation cascade switches from neutron to photon emission. The value of Q_min was set to 0.01 MeV in Ref. [2] and this remains the default value in FREYA. However, it was shown that using a large value of Q_min (1 MeV) in conjunction with a small T_S (0.2 MeV) was equivalent to using a small Q_min (0.01 MeV) with a large T_S (2.75 MeV).

Since then, several improvements have been made. While some have been reported in preliminary form elsewhere [4,5], others are described here for the first time.

In Ref. [7], we modified FREYA to conserve total angular momentum, including fluctuations of the dinuclear wriggling and bending modes, where the two fragments rotate in the same or opposite sense around an axis perpendicular to the dinuclear axis. The tilting and twisting modes, where the rotations are around the dinuclear axis, were neglected. These modes each contribute to fluctuations in the rotational energy, $\delta E_{\rm rot} = s_+^2/2\mathcal{I}_+ + s_-^2/2\mathcal{I}_-$, where wriggling is denoted by $+$ and bending by $-$. The moments of inertia for these modes (each of which is doubly degenerate), $\mathcal{I}_+$ and $\mathcal{I}_-$, are given in terms of the moments of inertia of the individual light and heavy fragments, $\mathcal{I}_L$ and $\mathcal{I}_H$, respectively, as well as moment of inertia for their relative motion, $\mathcal{I}_R$,

$$\mathcal{I}_+ = (\mathcal{I}_L + \mathcal{I}_H)\mathcal{I}/\mathcal{I}_R, \tag{1}$$

$$\mathcal{I}_- = \mathcal{I}_L\mathcal{I}_H/(\mathcal{I}_L + \mathcal{I}_H), \tag{2}$$

where $\mathcal{I} = \mathcal{I}_L + \mathcal{I}_H + \mathcal{I}_R$ is the total moment of inertia. The angular momenta of these rotational modes are sampled from thermal distributions characterized by the spin temperature T_S, $P_\pm(S_\pm) \propto \exp(-S_\pm^2/2\mathcal{I}_\pm T_S)$. The individual fragment angular momenta then follow. Any overall angular momentum S_0 (resulting from the absorption of an incoming neutron or the recoil from any prefission neutron emission) is also taken into account but the effect tends to be very small.

We express the spin temperature as $T_S = c_S T_{\rm sc}$, where the "scission temperature" $T_{\rm sc}$ is the temperature of the system at scission, and adopt c_S as a convenient parameter for controlling the overall magnitudes of the fragment angular momenta in FREYA. The general effect of changing c_S is similar to that of changing T_S in Ref. [2] and we shall discuss how the results depend on c_S. We note that if c_S is taken to be zero, the fragments emerge with only their share of the overall rotation, $S_{\rm f} = S_0\mathcal{I}_{\rm f}/\mathcal{I}$, which is usually very small (and is zero for spontaneous fission).

In the refined treatment of the statistical photon emission stage, we modulate the black-body spectrum by a giant dipole resonance (GDR) form factor, so that the prompt fission photon spectrum is

$$\frac{dN_\gamma}{d\epsilon_\gamma} \sim \frac{\Gamma_{\rm GDR}^2\epsilon_\gamma^2}{\left(\epsilon_\gamma^2 - E_{\rm GDR}^2\right)^2 + \Gamma_{\rm GDR}^2\epsilon_\gamma^2}\,\epsilon_\gamma^2 e^{-\epsilon_\gamma/T}, \tag{3}$$

from which the photon energy can readily be sampled. (Its direction is chosen isotropically, in the frame of the emitting fragment, as earlier.) As usual, T is the temperature of the emitting fragment. The position of the GDR is $E_{\rm GDR}$ (MeV) $= 31.2/A^{1/3} + 20.6/A^{1/6}$ [9], while its width is $\Gamma_{\rm GDR} = 5$ MeV. Relative to the earlier treatment [2], which employed pure black-body radiation, the inclusion of the GDR hardens the spectrum.

Furthermore, as a significant extension, we now include evaluated discrete transitions from the RIPL-3 database [10], as in Refs. [11,12]. The RIPL-3 library tabulates a large number of discrete electromagnetic transitions for nuclei throughout the nuclear chart. Some of these lines may be exploited experimentally to identify the specific fragment species. Unfortunately, complete information is available for only relatively few of the identified transitions, so some modeling is required to complement the tabulations (and this is done somewhat differently in the different codes). It is then possible to construct, for each product species, a table of the possible decays from the included discrete levels; see below.

The RIPL-3 data files are organized by element, with one file for each Z value, and each such file contains similarly structured listings for those isotopes of that element for which data exist. For any tabulated nucleus, we seek to include all levels in a complete level scheme, as indicated in the isotope header line on the data file. Each listed level ℓ may decay into a total of $n(\ell)$ lower levels $\{\ell'\}$ and the associated relative transition rate $P(\ell \to \ell')$ is indicated for each one, if available. Often the rate for a listed transition is not given and the corresponding transition is then ignored.

However, if all the decay rates from a given level ℓ are missing we assign decay rates from from that level to all of the lower levels ℓ' based on a simple phase-space consideration,

$$P(\ell \to \ell') \sim [\epsilon_\ell - \epsilon_{\ell'}]^2 e^{-(J_\ell - J_{\ell'})^2/2d_J^2}. \tag{4}$$

Here ϵ_ℓ is the energy of level ℓ, J_ℓ is its listed spin, and we take $d_J = 1$. It should be recognized that there are many more added transitions (201 568) than tabulated transitions (75 809). That is primarily because a level for which there are tabulated decay rates tends to decay to only some of the levels below it, whereas a level without tabulated decay rates is allowed to decay to *any* level below it and, furthermore, levels without tabulated decay rates tend to be high-lying and so have many lower levels.

In the previous de-excitation procedure, the product nucleus first made statistical emission until the yrast line was reached and then proceeded towards the ground state by collective emission. In order to better emulate the predominantly $E1$ and $M1$ character of the statistical transitions, it is assumed that the angular momentum of the fragment is reduced by $1\hbar$ for each emission. This is a somewhat idealized treatment which may need to be refined. In order to incorporate the subsequent discrete decays, we follow the earlier procedure until the total excitation has fallen below the highest discrete energy E_ℓ tabulated for that nucleus. The energy of the last statistical transition is then increased (slightly) to ensure that the last statistical decays leads to the closest lower-lying level and the further de-excitation is then carried out by means of the discrete rates described above. The emission of discrete photons is continued until the tabulated half life of a level exceeds a specified value $t_{\rm max}$.

If there are no RIPL-3 transitions available for a given product nucleus, the final de-excitation occurs as in Ref. [2] by emission of collective photons along the yrast line, with each emitted photon reducing the angular momentum by $2\hbar$.

We will show how the inclusion of the GDR modulation and the RIPL-3 transitions affect the photon observables. The maximum half life of the discrete levels, $t_{\rm max}$, as well as the minimum recorded photon energy, $g_{\rm min}$, have an impact on the generated photon energy and multiplicity, and we will explore how changes in these quantities affect the photon

observables obtained with FREYA. Because $g_{\min}$ represents the energy threshold for photon detection and $t_{\max}$ represents the time gate for the detectors, the comparison with a particular experiment depends on this information.

A. FREYA parameters

FREYA contains a number of physics-based parameters that affect various observables. They can be adjusted to available data. Here we give a brief description of their function and impact. The following six are code specific parameters:

(i) dTKE is a common, mass-independent, shift of the total fragment kinetic energy relative to the input TKE(A). This shift is tuned to give agreement with the average prompt neutron multiplicity $\overline{\nu}$, an adjustment that is typically of the order of one MeV or less.

(ii) x is the relative advantage in excitation energy given to the light fragment over the heavy fragment. This parameter significantly affects the neutron multiplicity as a function of fragment mass, $\nu(A)$. As shown in Ref. [8], it also affects the shape of the two-neutron angular correlation function. Other codes use systematics of excitation energy sharing [13] or tune the fragment temperature distribution to the available $\nu(A)$ data [11,12]. We have so far kept this parameter single-valued since we wish to address cases for which $\nu(A)$ is not available for tuning the temperature distribution.

(iii) c_T is the relative statistical fluctuation in the fragment thermal excitation. Prior to Ref. [8], c_T was assumed to be unity by default. In that work, however, it was shown that it had a significant effect on the width of the neutron multiplicity distribution $P(\nu)$ and, in particular, on the moments of $P(\nu)$ important for some applications. In addition, since the value of c_T adjusts the intrinsic excitation energy, the extra excitation energy must be taken away from the total kinetic energy of the fragments. Thus c_T effectively governs the width of the TKE distribution, $\sigma_{\rm TKE}$, as well.

(iv) e_0 sets the overall scale of the Fermi-gas level density parameter. (The asymptotic level density parameter is $a \sim A/e_0$.) It has only a negligible effect on the neutron multiplicity distribution, $P(\nu)$; the neutron multiplicity as a function of fragment mass, $\nu(A)$; the two-neutron angular correlation; and the photon observables. It does, however, affect the spectral shape of the prompt fission neutrons. We note that while the other parameters also affect the spectral shape and normalization to $\overline{\nu}$, the neutron spectrum is effectively the only observable dependent on e_0.

(v) c_S was defined previously as the ratio of the spin temperature T_S to the scission temperature $T_{\rm sc}$. It governs the overall magnitude of the fragment angular momenta. It affects the photon observables significantly, as we show here, whereas it has only a small effect on the neutron observables. However, there is a strong correlation between dTKE and c_S which serves to balance the neutron and photon multiplicities. If c_S is changed to match the photon multiplicity, dTKE must also be adjusted to maintain agreement with $\overline{\nu}$. This balance is most important for the multiplicities of prompt emission.

(vi) $Q_{\min}$ is defined as the energy above the neutron separation threshold where photon emission takes over from neutron emission. Since we adjust c_S to the photon multiplicity, this parameter is kept fixed at $Q_{\min} = 0.01$ MeV in the present studies.

The following two parameters are detector specific and not internal FREYA parameters:

(i) $g_{\min}$ is the minimum energy of photons that are being recorded and it is usually set to the minimum photon energy measurable by the photon detector in the measurement under analysis. Photons softer than $g_{\min}$ may still be emitted, they are just not being recorded in the particular event. This parameter is merely introduced for convenience and it does not affect the physical process.

(ii) $t_{\max}$ is the maximum half life of an energy level in the discrete part of the photon decay chain. If the photon cascade leads to a level that has a half life exceeding $t_{\max}$, the fragment is effectively stuck at that level during the time interval of the measurement and the subsequent history is immaterial. The effect of changing $t_{\max}$ is somewhat subtle and affects primarily photons emitted from low-energy levels having relatively low spin which are reached in the latter part of the decay cascade.

B. ^{252}Cf(sf) analysis

In Ref. [5], we adjusted dTKE, x, c_T, e_0, and c_S to several sets of data. These included the Mannhart spectral evaluation [14], the $P_n(\nu)$ distribution by Boldeman *et al.* [15], the $\nu(A)$ distribution determined by Dushin *et al.* [16], the neutron multiplicity as a function of TKE measured by Budtz-Jørgensen and Knitter [17], and the average total photon energy and the average total photon multiplicity measured by Billnert *et al.* [18]. While we later compared to the photon multiplicity distribution measured by the Detector for Advanced Neutron Capture Experiments (DANCE) [19], we did not include that distribution in the fits. Indeed, none of the current FREYA parameters affect the width of the photon multiplicity distribution $P_\gamma(N)$.

A wide range of possible parameter values were considered, with some physics bias to guide the fits. dTKE was varied from -5.0 to 5.0 MeV although large excursions from the measured mean would be in strong disagreement with data. The value of x was assumed to be larger than unity, limiting us to $1 < x < 1.5$ for the study. We choose $x > 1$ because the light fragment emits more neutrons on average than the heavy fragment in spontaneous and neutron-induced fission; see Ref. [6] for details. Also, given the limitations of the single-valued parameter x in describing the shape of $\nu(A)$ in the low and high fragment mass range, only the mass region $100 < A < 140$ was used in the fit. The parameter governing thermal fluctuations, c_T, was also assumed to be larger than unity, between 1 and 2. The value of the asymptotic level density parameter, e_0, was taken to be in the range $6 < e_0 < 12$ MeV. Finally, c_S was allowed to vary around unity, $0.5 < c_S < 1.5$. We will study larger excursions of c_S in Sec. IV to illustrate the magnitude of the effect. The comparison to data is made by calculating χ^2 for each data set individually and summing them to obtain the total χ^2.

In Ref. [5], the global χ^2 was minimized using a particle swarm algorithm. The best fit value using this method was found to give dTKE $= 0.5$ MeV, $x = 1.27$, $c_T = 1.08$, $e_0 = 10.37$ MeV, and $c_S = 0.87$. We note that some of these

values are not far from those suggested in Ref. [6], where photon observables were not yet included and $c_T \equiv 1$ by default: $e_0 \sim 10$ and $x = 1.3$. We are currently working on an approach that will give a better global χ^2, with well defined uncertainties for ^{252}Cf(sf), and will apply the same method to other spontaneously fissioning nuclei as well as neutron-induced fission. We note that this must be an ongoing process as new data are taken and become available.

For the results presented here, we use the best fit values of e_0 and c_S found in Ref. [5] for ^{252}Cf(sf) and keep these same values for our calculations of other cases. One might expect e_0 to be universal since it is independent of the fissioning nucleus. We have chosen to leave c_S fixed because it is strongly correlated with dTKE and its optimal value for a particular nucleus is therefore best determined on the basis of a global analysis of each isotope. To calculate results for neutron-induced fission, we adjust x based on $\nu(A)$ measurements, c_T based on $P(\nu)$ data, and fix dTKE to the measured $\overline{\nu}$. These parameter values, while still preliminary to some degree, provide benchmarks as to how well we can expect to describe the prompt fission photon data.

III. EFFECTS OF THE MODEL REFINEMENTS

We begin by showing how the FREYA photon emission results have evolved since the publication of Ref. [2]. That work considered unmodulated (black-body) statistical photon radiation,

$$\frac{dN_\gamma}{d\epsilon_\gamma} \sim \epsilon_\gamma^2 e^{-\epsilon_\gamma/T}, \tag{5}$$

until the yrast line was reached and the rotational energy was then dissipated by schematic photon emission along the yrast line. Thus no specific transitions were considered. In this section we compare three different model scenarios: (1) no GDR and no RIPL corresponding to the earlier treatment [2]; (2) GDR without RIPL, showing the effect of the modulation of the statistical decays without including the specific tabulated transitions; and (3) GDR with RIPL, corresponding to the improved treatment presented here.

All the calculations shown in this section are for ^{252}Cf(sf). The three different model scenarios all use the same parameter values, given in Sec. II B above with $g_{\min} = 0.10$ MeV and $t_{\max} = 1.5$ ns. Each calculation is based on one million FREYA events which suffices to ensure negligible statistical uncertainties aside from regions near the edges of phase space, either in the low and high A tails of the yields or close to symmetry for observables given as a function of fragment mass or at extreme values of total fragment kinetic energy where there are few events for observables given as functions of TKE.

Figure 1(a) shows the prompt photon energy spectrum over the full energy range. The calculation without the GDR modulation, from Eq. (5), drops exponentially and has a negligible yield already for photons of a few MeV. When the GDR modulation is included, the spectrum broadens significantly above 2 MeV and is about an order of magnitude larger in the tail region. The addition of the RIPL tables does not change the shape of the high-energy tail of the photon spectrum further. Instead, adding the tabulated RIPL transitions primarily affects the low-energy end of the spectrum, as shown for the distributions at energies less than 1 MeV in Fig. 1(b). In this region, the two calculations without the RIPL contributions are qualitatively similar, both being smooth and monotonically decreasing. The effect of including the RIPL tables can be clearly seen: the emission of low-energy photons is strongly reduced and a considerable degree of spectral structure appears in reflection of specific transitions in fragments with large yields.

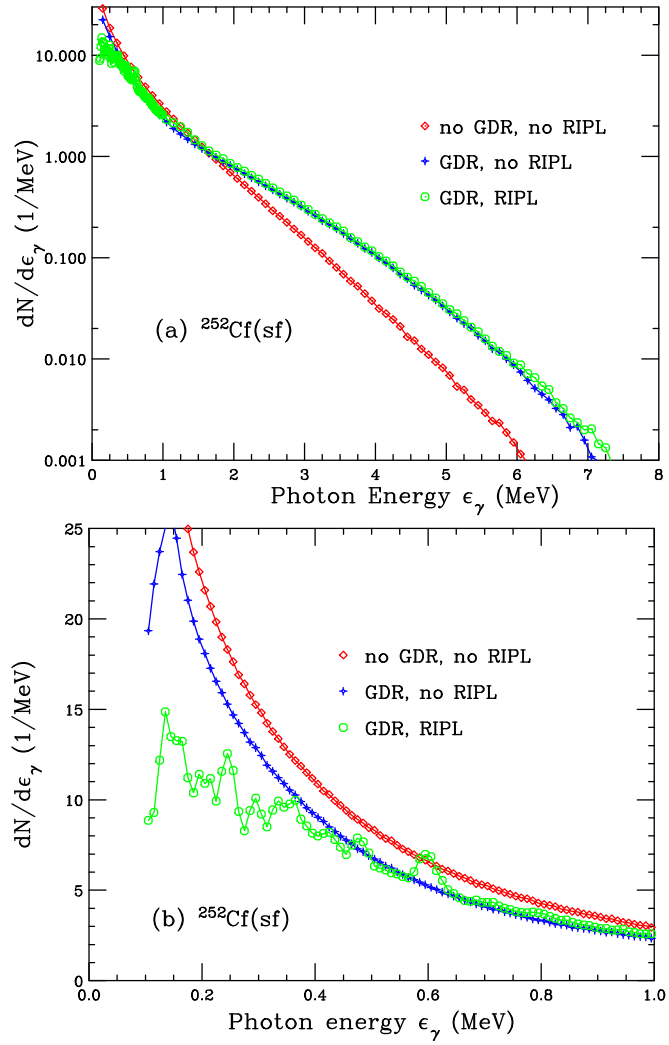

FIG. 1. The ^{252}Cf(sf) photon spectrum from FREYA calculated as in Ref. [2] without GDR form factor or RIPL-3 lines, with GDR but without RIPL-3 lines, and including both, as in the current version of FREYA. Panel (a) shows the spectrum over the entire energy range, while panel (b) shows the low-energy spectrum for photon energies less than 1 MeV. The calculated results in this and all subsequent figures are based on one million events and the associated sampling errors are shown. The spectra are normalized to the fission photon multiplicity.

Figure 2 shows the total photon energy E_γ and the photon multiplicity N_γ as functions of A, the mass number of the original (i.e., pre-evaporation) fragment nucleus, for the three

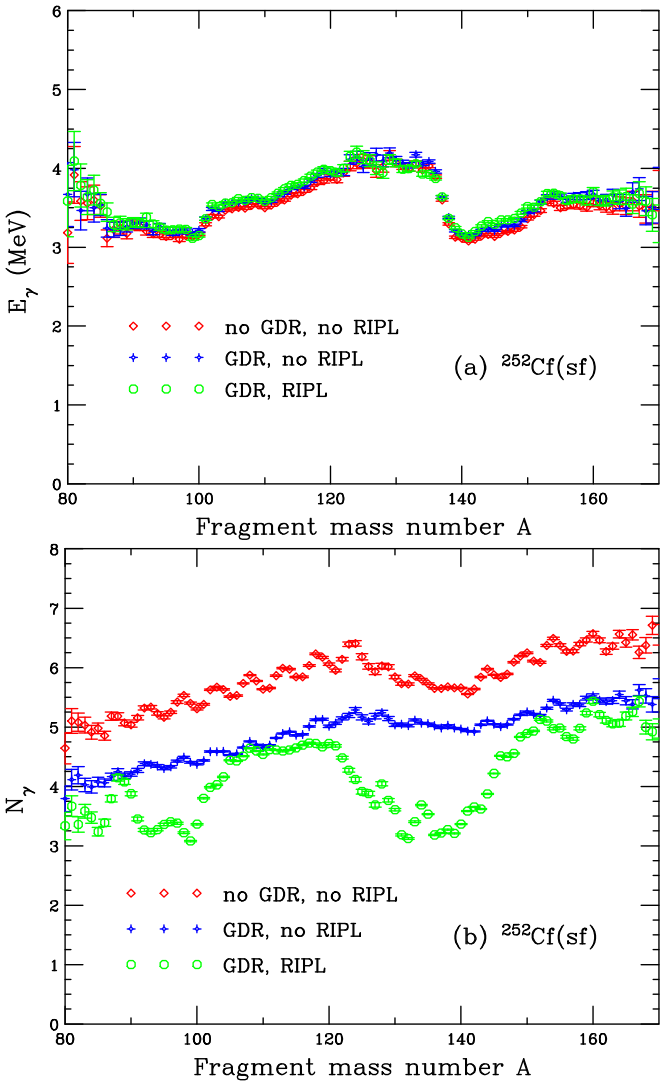

FIG. 2. The calculated fragment mass dependence of (a) the average total photon energy, $E_\gamma(A)$, and (b) the average photon multiplicity, $N_\gamma(A)$, for ^{252}Cf(sf) obtained with FREYA for three different model scenarios: (1) without GDR form factor or RIPL-3 transitions, as in the earlier FREYA [2]; (2) with the GDR form factor but without RIPL-3 lines; and (3) including both, as in the improved FREYA. Here and in subsequent figures, A is the mass number of the primary (i.e., pre-evaporation) fission fragment.

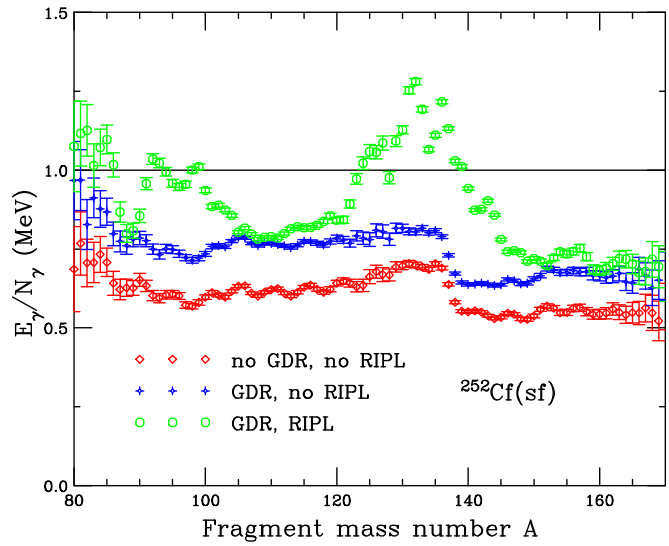

FIG. 3. The energy per photon as a function of fragment mass for ^{252}Cf(sf), $E_\gamma(A)/N_\gamma(A)$, obtained with FREYA for three different model scenarios: (1) without GDR form factor or RIPL-3 transitions, as in the earlier FREYA [2]; (2) with the GDR form factor but without RIPL-3 lines; and (3) including both, as done in the improved version of FREYA.

different scenarios. The total energy carried off by photons amounts to the excitation energy left over after neutron evaporation has ceased (apart from the small dependence on $t_{\max}$). Consequently, the total photon energy is practically unaffected by either the GDR modulation or the inclusion of discrete transitions, as seen in Fig. 2(a). Reflecting the A dependence of the neutron separation energy S_n, the total photon energy is relatively constant for $A < 100$ and $A > 150$ while, in the intermediate region, it increases slowly to a maximum near the doubly closed shell at $A = 132$ before dropping and then gradually rising again. It varies by around 1 MeV over the full A range. The shape of $E_\gamma(A)$ is similar to that of Ref. [2].

On the other hand, the photon multiplicity is affected more strongly by the inclusion of the GDR and the RIPL transitions, as seen in Fig. 2(b). Relative to the earlier treatment [2], the GDR modulation reduces the multiplicity by about one photon while still yielding a fairly smooth increase with the fragment mass A. In both scenarios, $N_\gamma(A)$ increases linearly (with a visible modulation arising, presumably, from pairing effects) until symmetry, $A = 126$, where the multiplicity decreases and then begins to rise again at $A \approx 140$. By contrast, the inclusion of discrete transitions has a large effect on the A dependence of N_γ. The transitions introduce more structure, including a more pronounced dip near the doubly closed shell at $A = 132$, similar to the "sawtooth" pattern in $\nu(A)$. However, contrary to that behavior, $N_\gamma(A)$ does not exhibit a pronounced sharp "tooth" in the light fragment mass region.

The energy per photon, shown in Fig. 3, is the ratio between the mean total photon energy per fission event E_γ, shown in Fig. 2(a), and the mean photon multiplicity N_γ per fission event, shown in Fig. 2(b). Because $E_\gamma(A)$ is unaffected by the GDR modulation and the inclusion of discrete transitions, the shape of the ratio is determined by the effect on $N_\gamma(A)$. All three scenarios show a change in the ratio at $A \approx 132$. Without the RIPL lines, there is simply a shift from a higher plateau for the lighter fragments to a lower plateau for the heavier fragments. But when the RIPL lines are included the pronounced dip in $N_\gamma(A)$ near $A \approx 132$ results in a peak in E_γ/N_γ quite different from the other two cases. It would be interesting to see how other implementations of the RIPL-3 tabulation (such as [11,12]) behave.

Figure 4 shows the total photon energy (emitted from both fragments) E_γ(TKE) (a) and the total photon multiplicity N_γ(TKE) (b) as functions of the total fragment kinetic energy TKE. The dependence here mirrors the fragment mass

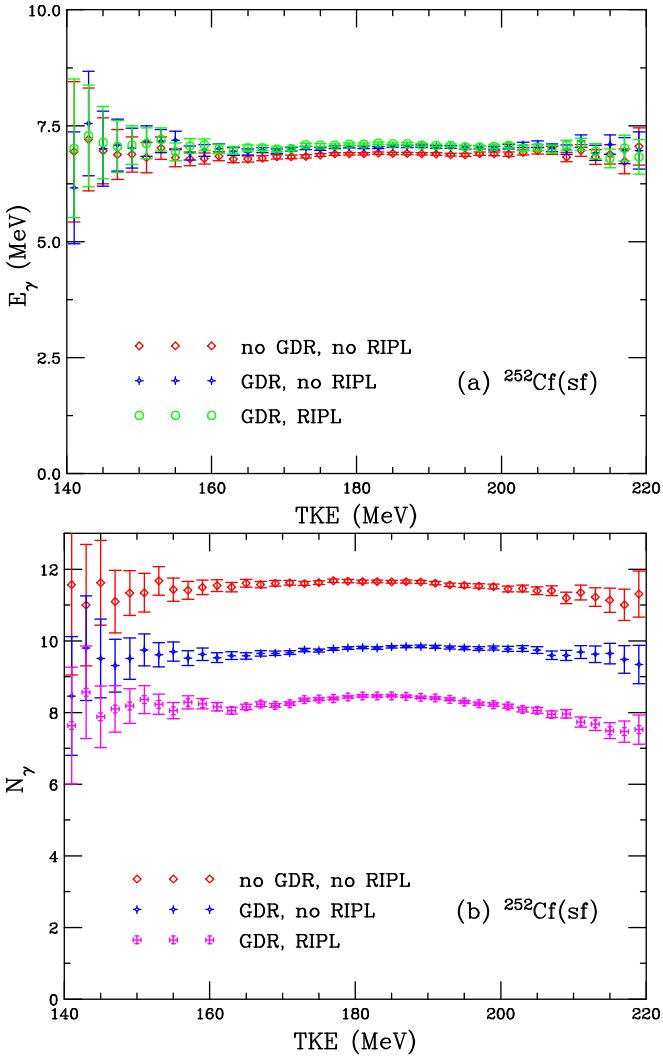

FIG. 4. The total photon energy E_γ (a) and the photon multiplicity N_γ (b) as functions of total fragment kinetic energy TKE calculated for ^{252}Cf(sf) with FREYA for three different model scenarios: (1) without GDR form factor or RIPL-3 transitions, as in the earlier FREYA [2]; (2) with the GDR form factor but without RIPL-3 lines; and (3) including both, as done in the improved version of FREYA.

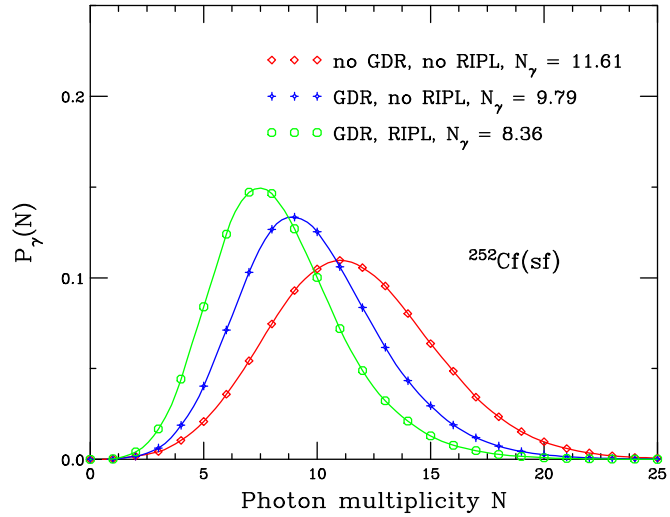

FIG. 5. The photon multiplicity distribution $P_\gamma(N_\gamma)$ for ^{252}Cf(sf) obtained with FREYA in three different model scenarios: (1) without GDR form factor or RIPL-3 transitions, as in the earlier FREYA [2]; (2) with the GDR form factor but without RIPL-3 lines; and (3) including both, as done in the improved version of FREYA.

dependence shown in Fig. 2: E_γ is insensitive to the spectral modulation and the RIPL lines, while N_γ decreases with both the modulation and the RIPL lines. Each model refinement reduces the multiplicity by nearly one photon. However, because the total kinetic energy is averaged over mass, there is no significant effect on the shape of N_γ(TKE).

Finally, Fig. 5 shows the total photon multiplicity distribution $P_\gamma(N)$ in the three model scenarios. Unlike the neutron multiplicity distribution $P_n(\nu)$, which does not have a Poisson form (primarily because of the dominant role played by the separation energy S_n), $P_\gamma(N)$ is more Poisson-like. The earlier FREYA treatment [2] yields the largest average photon multiplicity, $N_\gamma = 11.61$, while the GDR spectral modulation reduces the mean multiplicity to $N_\gamma = 9.79$, consistent with the fact that it tends to harden the spectrum (see Fig. 1). The inclusion of the discrete transitions reduces the multiplicity even further, to $N_\gamma = 8.36$.

After the above illustration of how the two main model refinements affect various photon observables, we now move on to discuss how the photon results of the improved FREYA depend on the various model parameters.

IV. DEPENDENCE ON c_S

In this section we discuss the effect on photon observables caused by changing the parameter c_S which controls the rotational motion of the fragments. We recall that the statistical energy available for neutron evaporation from a fragment is obtained by reducing its total excitation energy by the energy tied up in its rotation.

The other parameters are kept fixed while c_S is varied. We show results for $c_S = 0.2$, 0.8, 1.4, and 2.0. The value of 0.8 is rather close to the best fit value of 0.87. The value 0.2 is taken as a lower bound, significantly reducing the degree of rotation removing it altogether. The two larger values serve to illustrate the range of the effect.

Figure 6 presents $E_\gamma(A)$ and $N_\gamma(A)$ for the four illustrative values of c_S. As c_S is increased and the fragments are endowed with ever more rotation, there is less energy available for the neutrons. In Fig. 6(a), it can be seen that the photon energy simply seems to increment by approximately 0.5 MeV when c_S increases by 0.6. There is no visible mass dependence on changing c_S. However, the photon multiplicity does seem to show some modification of the fragment mass dependence with increasing c_S; see Fig. 6(b). While the general trend is the same for all values of c_S, there seems to be a larger increase in the multiplicity for the heavy fragment while the dip at $A \approx 132$ deepens with increasing c_S. In addition, there appears to be a rather flat plateau for the light fragment masses $100 < A < 120$ for $c_S = 0.2$ that acquires a positive slope as c_S increases.

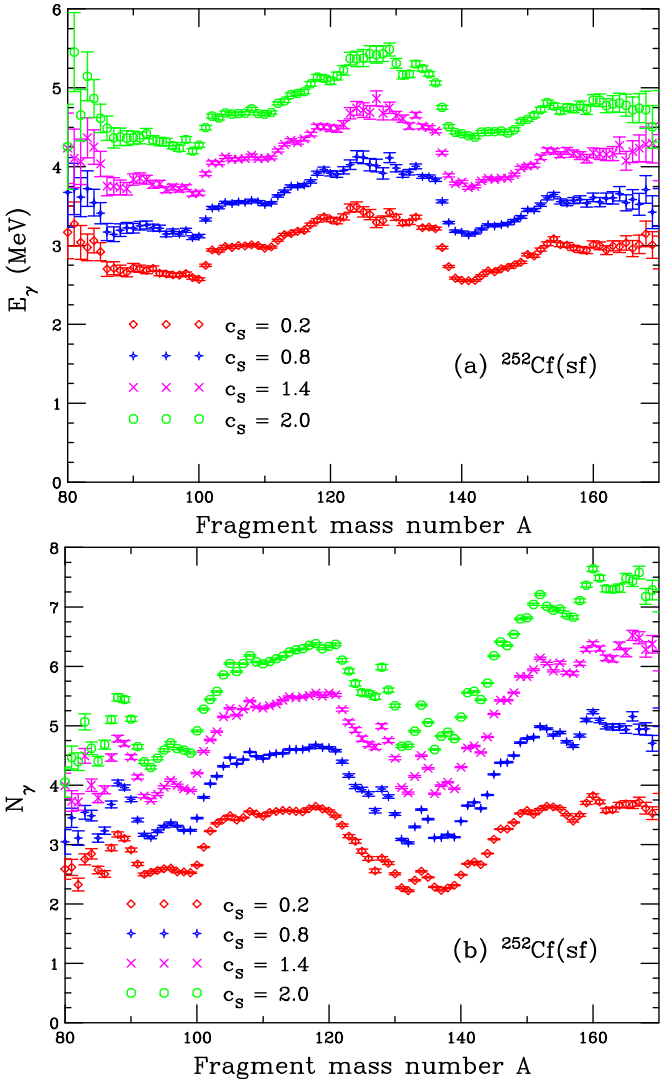

FIG. 6. The mean total photon energy E_γ (a) and the mean photon multiplicity N_γ (b) as functions of the fragment mass number A calculated for ^{252}Cf(sf) for four different values of the parameter c_S which sets the magnitude of the fragment spins. Results are shown for $c_S = 0.2$, 0.8, 1.4, and 2.0.

The changes in the photon multiplicity with fragment mass result in the observed differences in the energy per photon ratio shown in Fig. 7. The lowest value of c_S actually produces the most pronounced peak in E_γ/N_γ for $A \approx 132$. As c_S is increased, the energy per photon is reduced, particularly for the heavy fragment.

Figure 8 shows how the average magnitude of the fragment angular momentum, S_f, grows with the parameter c_S. The value of S_f is almost independent of fragment mass for $c_S = 0.2$, remaining near $2\hbar$. As c_S is increased, S_f and, thus, the portion of the excitation energy captured in rotational energy increases as well. $S_f(A)$ grows nearly linearly in the light mass region and then remains relatively constant in the heavy region. The increase in the light fragment spin grows more pronounced for larger values of c_S. The average values shown in Fig. 8 are consistent with those for secondary fragments (after neutron

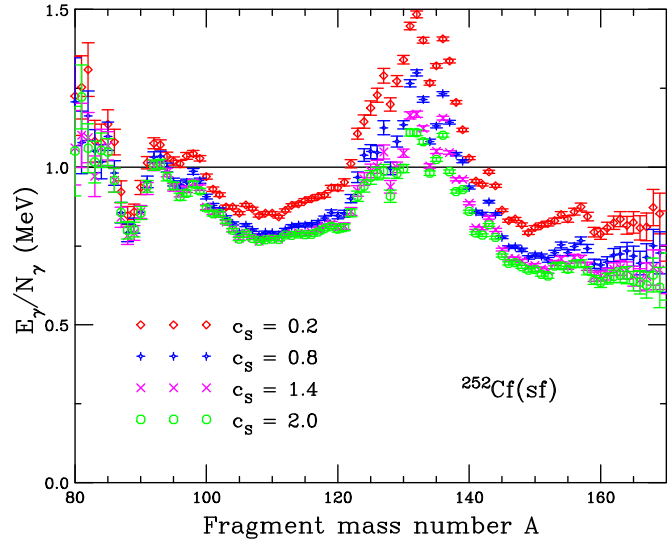

FIG. 7. The energy per photon E_γ/N_γ as a function of the fragment mass number A calculated for ^{252}Cf(sf) for four different values of the parameter c_S which sets the magnitude of the fragment spins. Results are shown for $c_S = 0.2$, 0.8, 1.4, and 2.0.

emission which has a negligible effect on fragment spin) for ^{252}Cf(sf) in Ref. [20].

We recall, however, that these results are calculated assuming that no other parameter value changes. Thus, if the total excitation energy is held fixed, increasing the rotational energy, as is the case for increased c_S, then less energy is available for neutron emission. Thus increasing c_S while keeping the other parameters fixed will decrease the average neutron multiplicity. For example, if all other parameters remain unchanged, the average neutron multiplicity can decrease by as much as 12% when c_S is increased from 0.2 to 2.0. Although

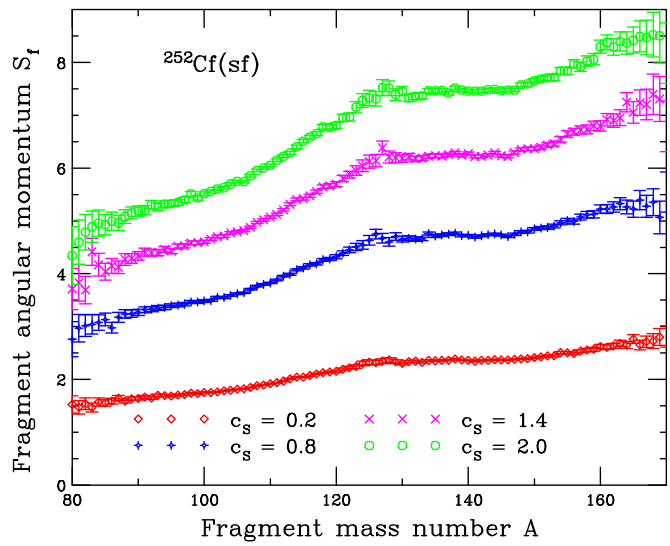

FIG. 8. The average fragment angular momentum S_f as a function of the fragment mass A for ^{252}Cf(sf) calculated for four different values of the parameter c_S (which controls the magnitude of the fragment spins). Results are shown for $c_S = 0.2$, 0.8, 1.4, and 2.0.

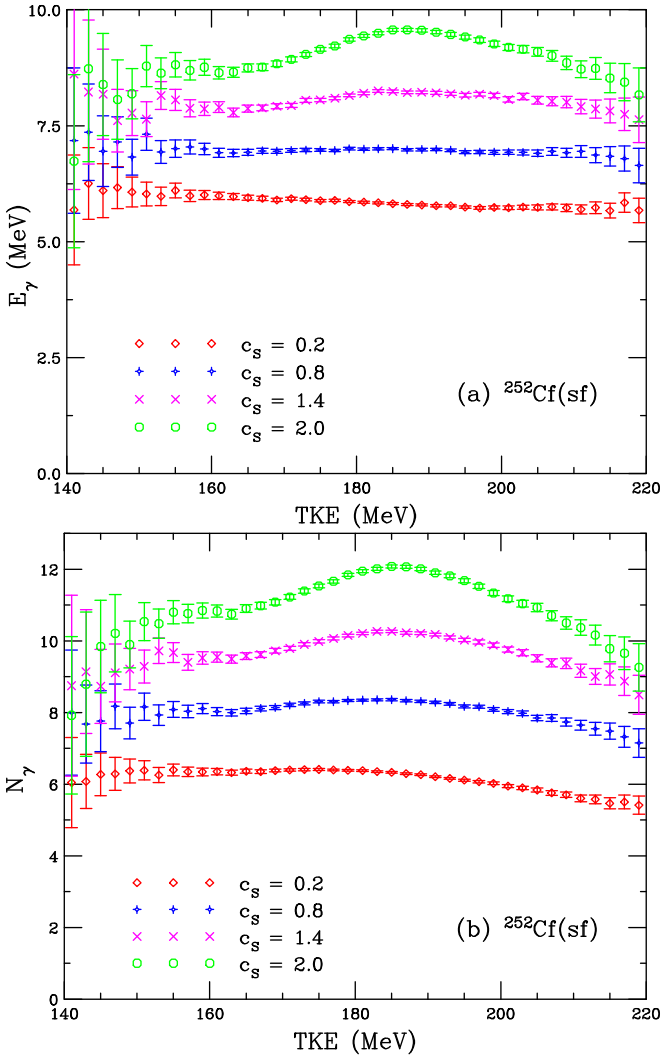

FIG. 9. The total photon energy E_γ (a) and the photon multiplicity N_γ (b) as functions of total fragment kinetic energy TKE for ^{252}Cf(sf) calculated for four different values of the parameter c_S (which controls the magnitude of the fragment spins; see Fig. 8). Results are shown for $c_S = 0.2$, 0.8, 1.4, and 2.0.

this could be compensated for by changing the value of dTKE, one has to be careful to adjust it within reasonable physics limits. Furthermore, when adjusting variables it is important to check the effect on other observables to ensure that overall description remains good. The results here are thus for illustrative purposes only.

Figure 9 shows the variation of E_γ(TKE) and N_γ(TKE) with respect to c_S. As c_S is increased, the these functions develop some curvature with an enhancement appearing around TKE $\approx$ 190 MeV.

Finally, the c_S dependence of the photon multiplicity distribution $P_\gamma(N)$ is shown in Fig. 10. As c_S is increased, the fission fragments are formed with ever larger angular momenta and because these remain largely unchanged during the neutron evaporation chain, the resulting postevaporation fragments tend to have correspondingly higher excitations.

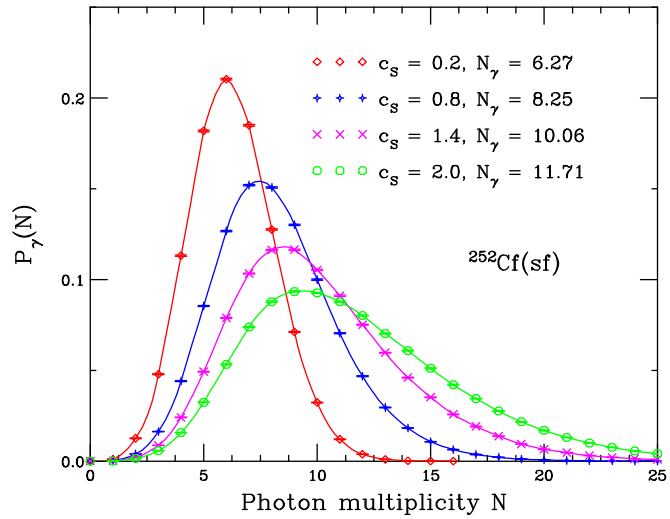

FIG. 10. The photon multiplicity distribution $P_\gamma(N)$ for ^{252}Cf(sf) calculated for four different values of the parameter c_S (which sets the magnitude of the fragment spins). Results are shown for $c_S = 0.2$, 0.8, 1.4, and 2.0 using $g_{\min} = 0.1$ MeV and $t_{\max} = 10$ ns. The mean multiplicity for each value of c_S is indicated.

Consequently, a larger number of photons may be emitted, increasing both the mean multiplicity and the width of $P_\gamma(N)$.

V. DEPENDENCE ON $g_{\min}$ AND $t_{\max}$

Here we discuss the dependence of the FREYA results on the detector-related parameters $g_{\min}$ and $t_{\max}$. In our discussion of the dependence on $g_{\min}$, we show results similar to those in Sec. IV. We refer to photons above $g_{\min}$ as detected fission photons since photons with energies below $g_{\min}$, while emitted, will not be detected. The effect of the detection time window, $t_{\max}$, is more subtle, however, so we present the $t_{\max}$ dependence relative to an infinitely wide detection window, $t_{\max} \to \infty$. While most of the results in this section are shown only for ^{252}Cf(sf), some results for ^{235}U($n_{\rm th}$,f) and ^{239}Pu($n_{\rm th}$,f) are included as well. It should be recognized that neither of these quantities affects the physical photon emission, only the recording of the emission.

A. Dependence on $g_{\min}$

We begin by considering values of $g_{\min}$ that are in the range of typical photon detectors, 0.05–0.20 MeV. We show the dependence of the total photon multiplicity N_γ on the total fragment kinetic energy TKE. We then illustrate the effect of increasing $g_{\min}$ up to 2 MeV which puts the focus ever more on the high-energy (and, hence, mostly statistical) photons.

The effect on $E_\gamma(A)$ is very small, with a change in $g_{\min}$ between 0.05 and 0.20 MeV producing a reduction of only $\approx$ 2%, and it is therefore not shown in a separate figure, whereas the $g_{\min}$ dependence of $N_\gamma(A)$ and $E_\gamma(A)/N_\gamma(A)$ are shown in Figs. 11(a) and 11(b), respectively.

The effect on the photon multiplicity is significant (albeit not as large as changing c_S by a factor of 10, between 0.2 and 2, as shown in Fig. 10). If $g_{\min} \to 0$, ever more soft photons

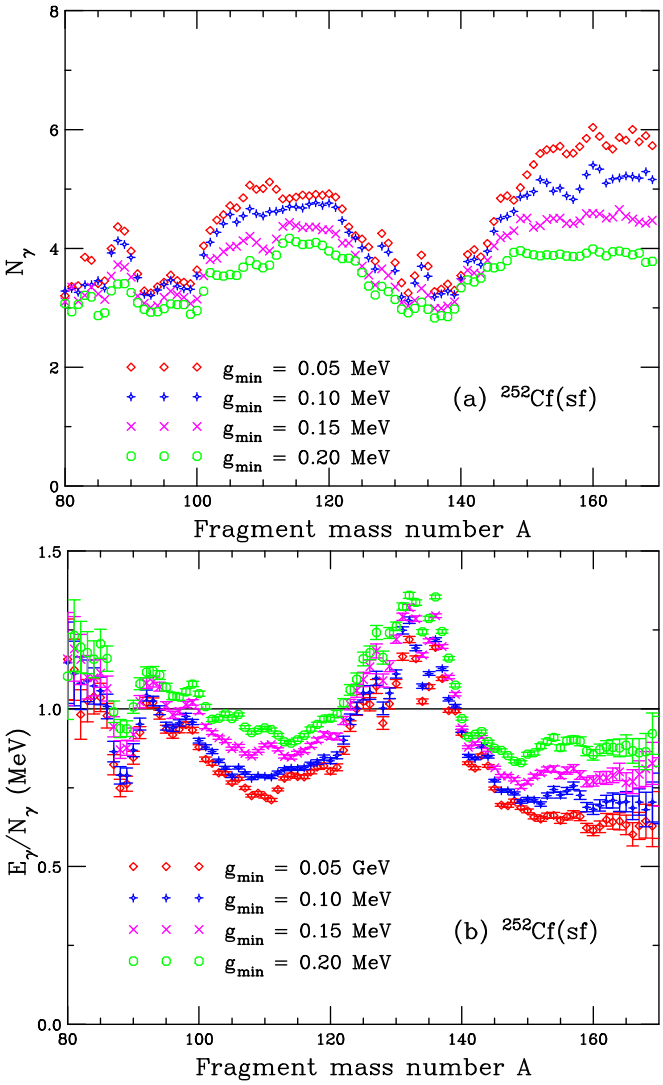

FIG. 11. The photon multiplicity N_γ (a) and the energy per photon E_γ/N_γ (b) as functions of fragment mass number A for ^{252}Cf(sf) calculated for four different values of $g_{\min}$, the minimum photon energy detected. Results are shown for $g_{\min} = 0.05$, 0.10, 0.15, and 0.20 MeV.

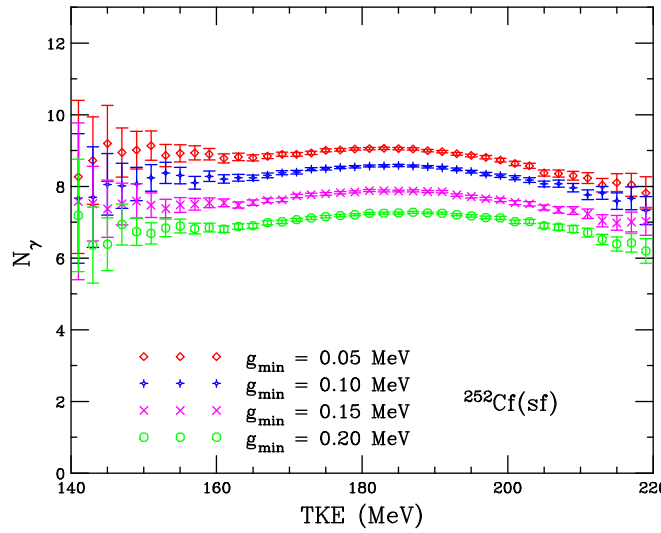

FIG. 12. The average photon multiplicity N_γ as a function of total fragment kinetic energy TKE calculated for ^{252}Cf(sf) for four different values of the parameter $g_{\min}$, the minimum photon energy detected. Results are shown for $g_{\min} = 0.05$, 0.10, 0.15, and 0.20 MeV.

could be emitted, increasing the total multiplicity. The photon multiplicity from the heavy fragment is affected the most by a change in $g_{\min}$, with a $\approx 50\%$ change in N_γ near $A = 160$ relative to a $\approx 20\%$ change near $A = 110$. Because the discrete transitions tend to be relatively soft, their significance will diminish rapidly as $g_{\min}$ is increased. There are also soft statistical photons at small $g_{\min}$ that will be removed from the multiplicity count. As a result, the dependence of N_γ on A will grow ever weaker until it is effectively constant.

Figure 11(b) shows the dependence of $E_\gamma(A)/N_\gamma(A)$ on $g_{\min}$. Also here the A dependence weakens as $g_{\min}$ is increased. However, the characteristic shape shown in the previous sections remains relatively unchanged.

For the same values of $g_{\min}$, Fig. 12 displays the multiplicity N_γ as a function of the total kinetic energy TKE. While the total photon energy is generally independent of TKE for ^{252}Cf, there is a mild TKE dependence of the total photon multiplicity. The main effect of increasing the detection threshold $g_{\min}$ is an overall reduction in N_γ.

We now show the dependence of E_γ and N_γ on $g_{\min}$ over a significantly broader range of values, up to 2 MeV. These results are shown in Fig. 13 for ^{252}Cf(sf), ^{235}U($n_{\rm th}$,f) and ^{239}Pu($n_{\rm th}$,f). Figure 13(a) shows that the slow decrease, noted above for $g_{\min} < 0.2$ MeV, grows stronger for larger values of $g_{\min}$. The dependence is approximately linear for all three systems. The dropoff of E_γ is somewhat steeper for ^{252}Cf(sf) than for ^{235}U($n_{\rm th}$,f) and ^{239}Pu($n_{\rm th}$,f) whose slopes are very similar.

When $g_{\min}$ is small, the detected total fission photon energy approaches its maximum possible value, namely the total radiated photon energy. For each product nucleus, the radiated photon energy is given by its total excitation energy after neutron evaporation has ceased which is typically 2–3 MeV below the threshold at $E^* = S_n \approx 6$ MeV. As $g_{\min}$ is increased from 0.05 to 2 MeV, E_γ decreases by a factor of 2.5–3, corresponding to a couple of MeV for each product nucleus.

Because most of the radiated photons are relatively soft, the detected fission photon multiplicity N_γ drops off significantly more rapidly as the threshold $g_{\min}$ is increased, as seen in Fig. 13(b). Again, the dependence on $g_{\min}$ is stronger for ^{252}Cf(sf) which also starts out from a somewhat higher value at $g_{\min} \approx 0$ than the other two cases displayed. By $g_{\min} > 0.5$ MeV, all three cases show essentially the same $N_\gamma(g_{\min})$ which decreases to slightly less than 1 by $g_{\min} = 2$ MeV.

The similarity in photon multiplicity is likely due to the fact that (in the current version of FREYA) no photons are emitted until the excitation energy of the fragment has fallen below the neutron separation energy. As already mentioned in the Introduction, this has the consequence that neutron observables are insensitive to the choice of $g_{\min}$ and $t_{\max}$. Due

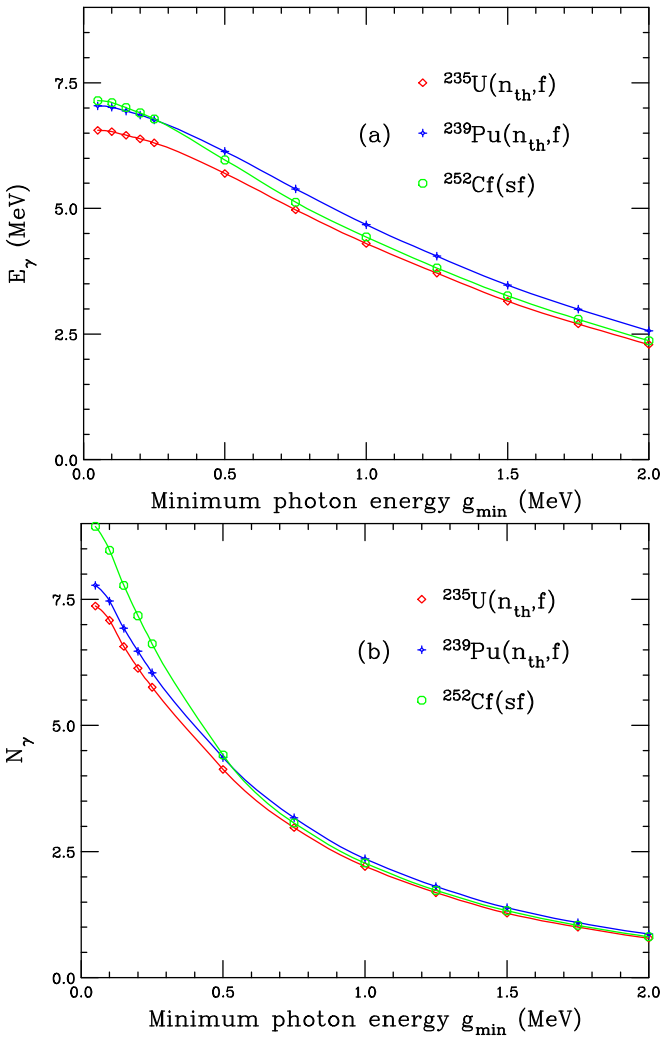

FIG. 13. The total photon energy E_γ (a) and the photon multiplicity N_γ (b) calculated for ^{235}U($n_{\rm th}$,f), ^{230}Pu($n_{\rm th}$,f), and ^{252}Cf(sf) as a function of the photon energy cutoff $g_{\rm min}$. The value of $t_{\rm max}$ was 10 ns for all cases.

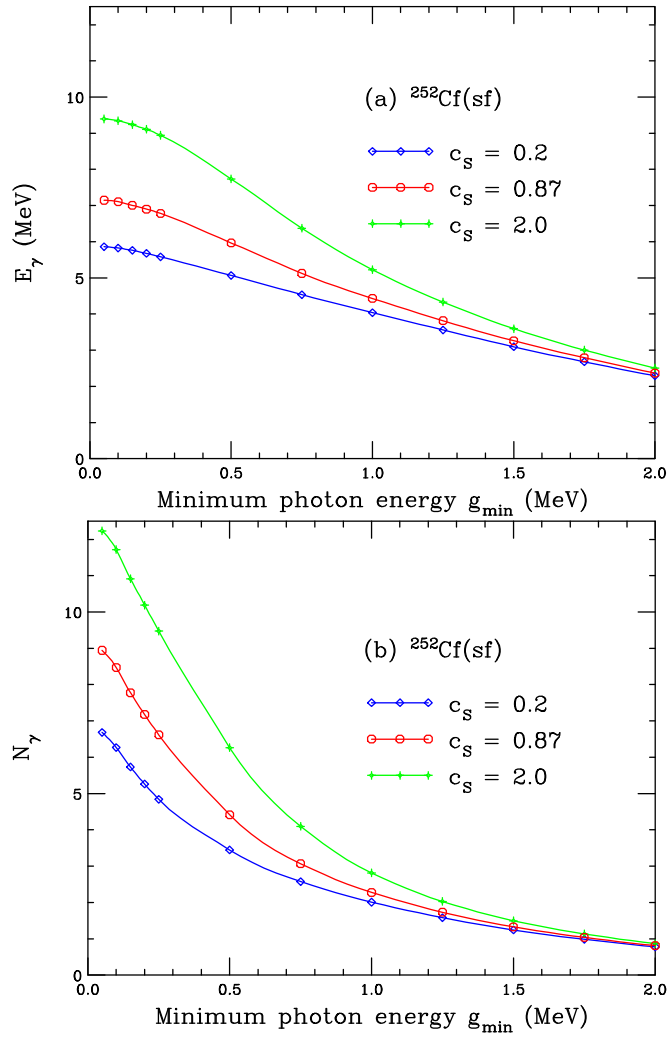

FIG. 14. The total photon energy E_γ (a) and the photon multiplicity N_γ (b) calculated for ^{252}Cf(sf) as a function of photon energy cutoff $g_{\rm min}$ for three values of c_S: $c_S = 0.2$, 0.87, and 2.0. The value of $t_{\rm max}$ was 10 ns.

to this, one may also expect that the residual excitation energy left for photon emission has a weak dependence on incident neutron energy, as already mentioned in previous work [2,6].

We also note that the similarities between the three cases shown may be due in part to the use of the same values of c_S, namely the one determined by the preliminary fit to ^{252}Cf(sf) data. A fit of c_S to the data available for additional cases may result in a greater range of E_γ and N_γ at $g_{\rm min} \approx 0$.

The total detected fission photon energy E_γ is shown in Fig. 14(a). For $c_S = 0.2$, E_γ decreases approximately linearly with increasing $g_{\rm min}$. As c_S is increased, the fission fragments are created with ever larger angular momenta and the associated rotational energy is eventually disposed of by radiation of relatively soft photons. Consequently, E_γ goes up as well. The effect is about 50% in the ideal case when the detection threshold $g_{\rm min}$ vanishes. When $g_{\rm min}$ is increased, an ever larger proportion of these soft photons are not seen. Thus the sensitivity to c_S diminishes.

Figure 14(b) shows the corresponding results for the detected total fission photon multiplicity, which has a stronger dependence on $g_{\rm min}$, as noted already in the discussion of Fig. 14(a). The dependence is particularly strong for the lowest values of $g_{\rm min}$ where, for $c_S = 2$, increasing $g_{\rm min}$ from 0.1 to 0.2 MeV reduces N_γ by $\sim 20\%$, while increasing c_S from 0.2 to 2 decreases N_γ by nearly a factor of 2 in the same region of $g_{\rm min}$. Thus the dependence of N_γ on $g_{\rm min}$ is more power-law like. As was the case for E_γ, when $g_{\rm min}$ is increased, N_γ becomes independent of c_S because, as $g_{\rm min}$ approaches 2 MeV, effectively only a single (likely statistical) photon has sufficient energy to be detected.

Last, we show the dependence of the energy per photon, E_γ/N_γ, on the detection threshold $g_{\rm min}$ for the same values of c_S. The energy per photon is almost independent of c_S, as shown in Fig. 15. It exhibits an almost linear increase with $g_{\rm min}$. Starting out from slightly below 1 MeV for low $g_{\rm min}$, E_γ/N_γ becomes greater than 1 MeV at $g_{\rm min} \approx 0.15$ MeV for $c_S = 0.2$ and at $g_{\rm min} \approx 0.25$ MeV for $c_S = 2$. Thus already for

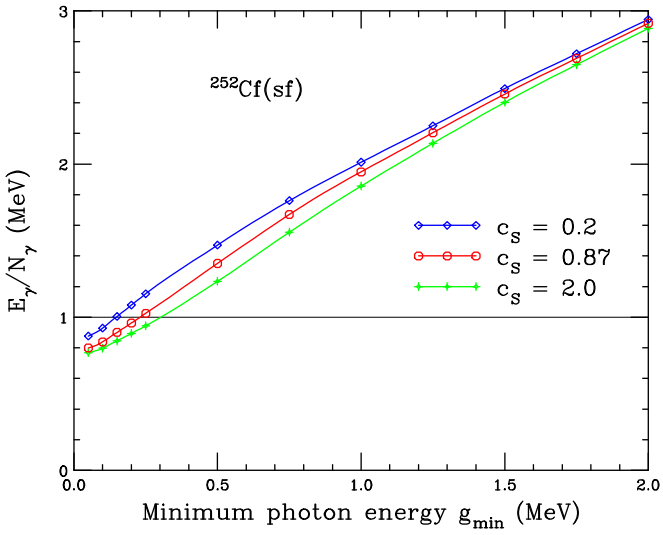

FIG. 15. The energy per photon E_γ/N_γ calculated for ^{252}Cf(sf) as a function of the photon energy cutoff $g_{\min}$ for three values of c_S: $c_S = 0.2$, 0.87, and 2.0. The value of $t_{\max}$ was 10 ns taken as for all cases.

thresholds $g_{\min}$ far below 1 MeV, each detected fission photon carries over 1 MeV of energy on average.

B. Dependence on $t_{\max}$

With the inclusion of the discrete transitions from the RIPL-3 library in FREYA, it has become possible to study the effect of the time window in which the detector operates on the measured photon spectrum which is expected to be particularly significant at low energies. For example, if the photon cascade from a fission product arrives at a long-lived isomeric state, the decay chain may not proceed further during the measurement time and no more prompt photon emission can be detected from that nucleus.

Because the fission fragment distributions differ for ^{252}Cf(sf), ^{235}U($n_{\rm th}$,f), and ^{239}Pu($n_{\rm th}$,f), it is instructive to look at how N_γ and E_γ change as the detection time window is varied. The effect for ^{252}Cf(sf) should be notably different from the effects for ^{235}U($n_{\rm th}$,f) and ^{239}Pu($n_{\rm th}$,f) because the light fragments are shifted upwards in mass for the former case relative to the latter ones. In addition, the wings of the fragment mass distribution are broader for ^{252}Cf and the dip in the symmetric region is less pronounced. All these differences could lead to a significantly different population of the relevant isomeric states. Furthermore, N_γ should be more affected than E_γ because the isomeric states are encountered relatively far down the cascade so the photons affected are rather soft and will not strongly affect E_γ.

Figure 16 shows the dependence of N_γ and E_γ on the effective detector time window $t_{\max}$ for all three cases, employing a detection threshold of $g_{\min} = 0.1$ MeV. The extracted value for a given $t_{\max}$ is shown relative to the corresponding value obtained with an effectively infinite time window, $t_{\max} = 5$ μs. Thus the ratio represents a cumulative value of the multiplicity or energy as a function of the duration

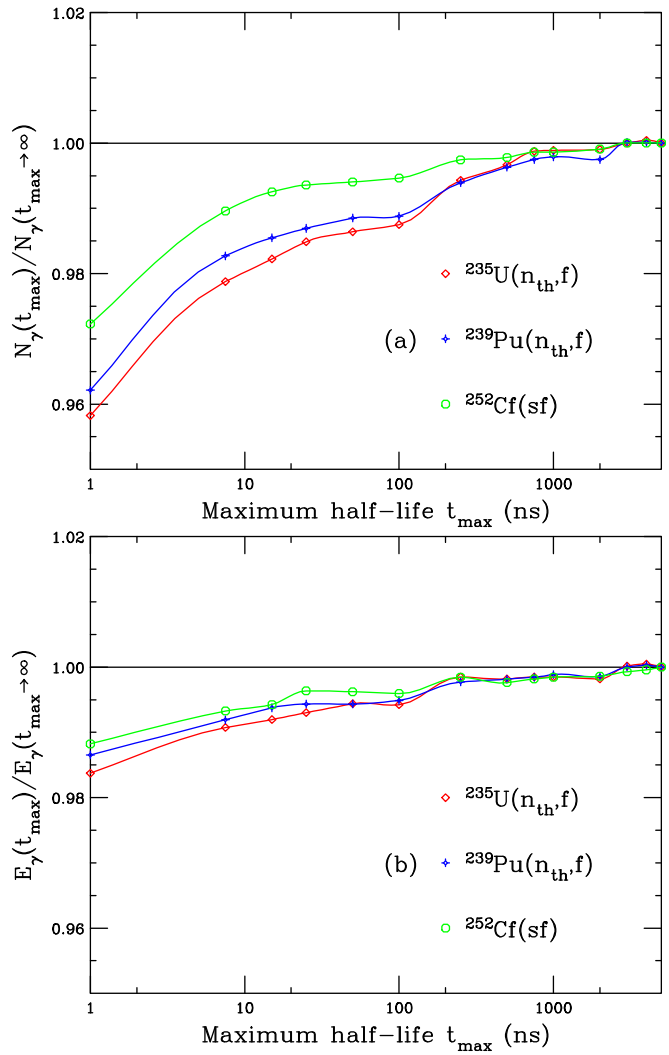

FIG. 16. The total photon energy (a) and the photon multiplicity (b) as functions of the maximum level half life $t_{\max}$, relative to the results for $t_{\max} \to \infty$ (effectively $t_{\max} = 5$ μs), for ^{235}U($n_{\rm th}$,f), ^{230}Pu($n_{\rm th}$,f), and ^{252}Cf(sf).

of the detector time window. As expected, there is a noticeable difference between the three cases for the multiplicity ratios; see Fig. 16(a). The differences are largest for the shortest time windows, with the ratio being largest for ^{252}Cf. All are very close to unity for $t_{\max} > 500$ ns. On the other hand, as also expected, the $t_{\max}$ dependence of the ratios for the total photon energy are very similar for the three cases; see Fig. 16(b).

Our results differ somewhat from those obtained with the CGMF code [21]. There are a number of ways these differences could arise. First, while both treatments start from the same fission fragment yields and the same average total kinetic energies [22], FREYA assumes that the charge distribution has a normal form (with the experimentally measured charge variance), whereas CGMF invokes Wahl systematics which takes account of odd-even effects. Second, FREYA does not use the measured width of the TKE distribution but generates it from the thermal fluctuations in the excitation energy (controlled by the c_T parameter). Third, FREYA employs the single-valued

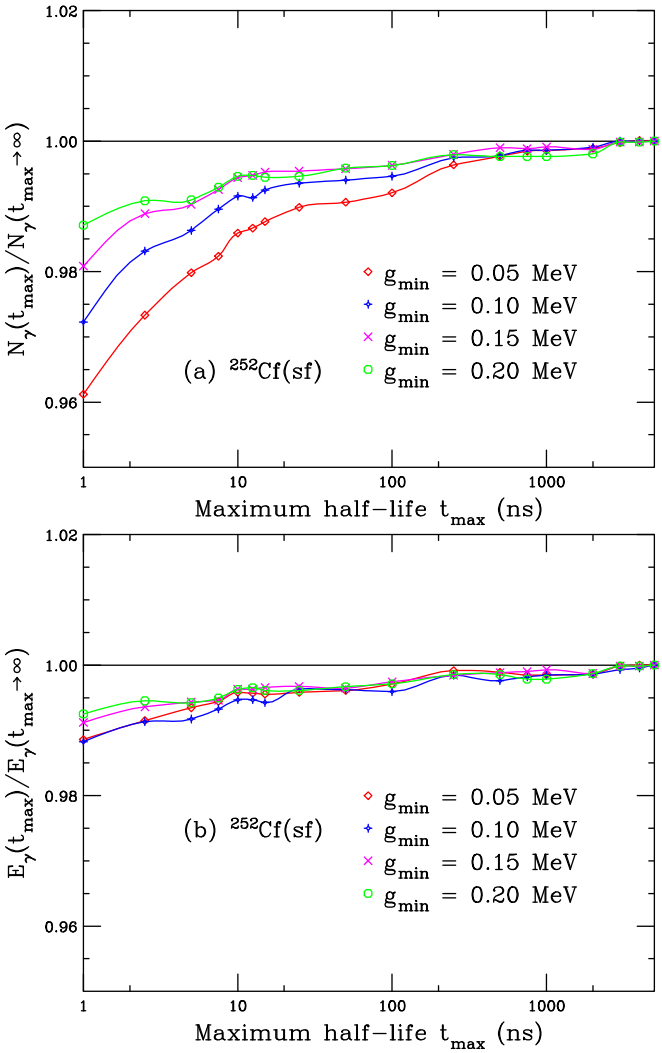

FIG. 17. The total photon energy (a) and the photon multiplicity (b) as functions of the maximum level half life t_{max}, relative to the results for $t_{max} \to \infty$, for ^{252}Cf(sf) using $g_{min} = 0.05, 0.10, 0.15$, and 0.20 MeV.

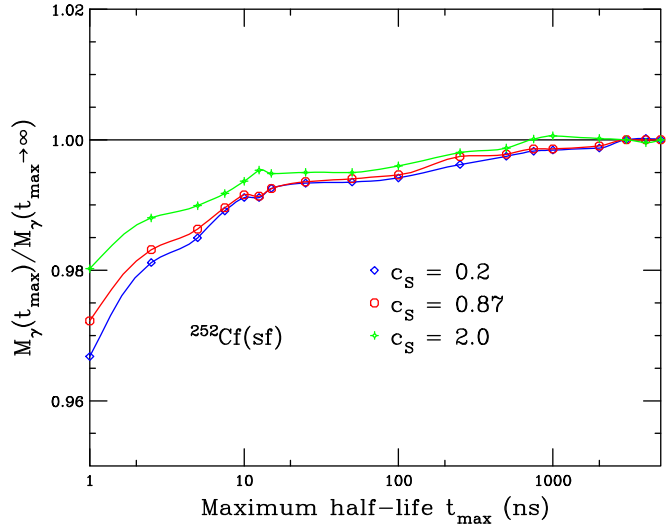

FIG. 18. The total energy per photon, E_γ/N_γ, as a function of the maximum level half life t_{max}, relative to the results for $t_{max} \to \infty$, for ^{252}Cf(sf) using $c_S = 0.2$, 0.87 (the default value), and 2.0.

parameter x for the sharing of excitation energy between the fragments, while CGMF adjusts the fragment temperature point by point to better reproduce $\nu(A)$ [23].

Fourth, CGMF uses the Hauser-Feshbach treatment for the fragment decays, while FREYA uses a Weisskopf-Ewing spectrum for neutron emission followed by the photon cascade as described in Sec. II. Finally, and perhaps most important, the resulting ratio depends on how the RIPL-3 lines are implemented: because the tables are rather incomplete a significant degree of modeling is required to complement the measured information, especially on branching ratios, and the two codes employ different methods for that. (For the CGMF treatment, see Refs. [24,25].) Of course, the results also depend on the specific value of g_{min} employed.

To show how these ratios could change with inputs, we look first at $N_\gamma(t_{max})$ and $E_\gamma(t_{max})$ for different values of g_{min}, as shown in Fig. 17. We focus on ^{252}Cf(sf) and choose relatively low values of g_{min}, from 0.05 to 0.20 MeV. Again the largest effect is on the multiplicity, shown in Fig. 17(a), and for $t_{max} \leqslant 100$ ns. The greatest difference is between $g_{min} = 0.05$ MeV and 0.10 MeV. Higher values of g_{min} have a smaller effect because the discrete levels tend to emit rather soft photons. This is evident from the cumulative total photon energy shown in Fig. 17(b) which is almost independent of g_{min}.

Figure 18 shows the cumulative multiplicity $N_\gamma(t_{max})$ for several values of c_S. The value $c_S = 0.87$ is the best fit value from the ^{252}Cf(sf) fit [5], and is the same as the results shown in Fig. 16(a) for ^{252}Cf and in Fig. 17(a) for $g_{min} = 0.10$ MeV. The other two values, $c_S = 0.2$ and $c_S = 2$, are the upper and lower limits used in the calculations shown in the previous section. The dependence on c_S is weaker than that on g_{min}. Indeed, it is sufficiently weak to make it unnecessary to show the c_S dependence of the cumulative total photon energy $E_\gamma(t_{max})$.

Interestingly, the change in the cumulative multiplicity ratio is largest for the lowest c_S value which represents the lowest rotational energy, while the effect is reduced for $c_S = 2$. Perhaps it is less likely that the long-lived isomeric states are being populated when the initial angular momentum is higher (see Fig. 8).

VI. COMPARISON TO DATA

We now turn to a comparison of the default FREYA results which use $c_S = 0.87$ as determined from the fit to ^{252}Cf(sf) data [5]. We use $g_{min} = 0.1$ MeV and $t_{max} = 10$ ns unless otherwise specified.

A. ^{252}Cf(sf)

We will compare the FREYA calculations to several previous experiments. Those by Nifenecker *et al.* [26] and Nardi *et al.* [27] took data on photon energy as a function of fragment mass and total kinetic energy. Photon multiplicities as functions of fragment mass were measured by Pleasonton *et al.* [28] and

Johansson *et al.* [29]. All these experiments were completed before the mid 1970s.

More recent experiments have not yet correlated photon production with fragment mass or kinetic energy. Billnert *et al.* [18] measured the prompt fission photon spectrum at IRMM in Belgium. The DANCE experiment at the Los Alamos Neutron Science Center reported the photon multiplicity distribution [19] while the Livermore-Berkeley Array for Collaborative Experiments (LiBerACE) experiment at LBNL studied neutron-photon correlations by measuring the photon multiplicity distribution for two or four neutrons emitted [30].

Nifenecker *et al.* [26] placed the ^{252}Cf source and the fragment detectors in the center of a spherical gadolinium-loaded liquid scintillator tank 1 m in diameter. The neutrons were distinguished from photons by timing: the photon pulse came first, followed several microseconds later by neutrons. The pre-evaporation mass and kinetic energy of each fragment was deduced from the number of neutrons emitted. Since they could not determine which fragment emitted the photons, they reported the average photon energy from both fragments as a function of the light fragment mass A_L and total fragment kinetic energy.

Nardi *et al.* [27] used a thin ^{252}Cf source placed inside a vacuum chamber with fragment detectors on both sides, also in the chamber. The photons were detected with plastic scintillators that were placed 60 cm from the source, behind the fragment detectors and outside the chamber. They separated photons from neutrons using time-of-flight techniques. Because their geometric acceptance was small, they were able to measure the total energy release due to photon emission from individual fragments, which was not possible in Nifenecker's 4π geometry. Thus Nardi *et al.* could report E_γ for each individual fragment mass, while Nifenecker *et al.* could report only the total E_γ emitted from both fragments combined.

These results are shown in Fig. 19. The data as a function of A from Nardi *et al.* [27] are shown in Fig. 19(a). The agreement of the calculations with the data is generally very good, especially given the uncertainties on the data. The exceptions are the two heavy fragments closest to a symmetric mass split. In Fig. 19(b), we show the combined total photon energy from the two fragments as a function of the light fragment mass, A_L. The only uncertainties on the Nifenecker points are those representing a typical full width at half maximum of each A_L, shown at $A_L = 92$, 108, 120, and 125. If these representative uncertainties are considered at all A_L, the Nifenecker data are in relatively good agreement with both the FREYA calculations and the Nardi data. The large uncertainties on the Nardi data come from summing the uncertainties on A_L and A_H when folding the data from panel (a) over to obtain the total mean E_γ per fission event rather than E_γ per fragment.

As is also apparent from Fig. 19(b), the uncertainties in the FREYA calculation are the largest where the yields are the lowest, namely near symmetry ($120 < A_L < 126$) and, particularly, in the tails of the distributions ($A_L < 100$). Increasing the number of events above one million would of course reduce the uncertainties correspondingly, but the trend will remain unchanged. We note that the rise in E_γ in the calculation for $A_L > 115$ corresponds to the rather abrupt decrease in E_γ between $A \sim 132$ and $A \sim 140$ shown in Fig. 19(a). Given the relatively large uncertainties in the Nardi data and the implied uncertainties in the Nifenecker data (where shown), it would be useful to repeat these measurements with more modern detectors.

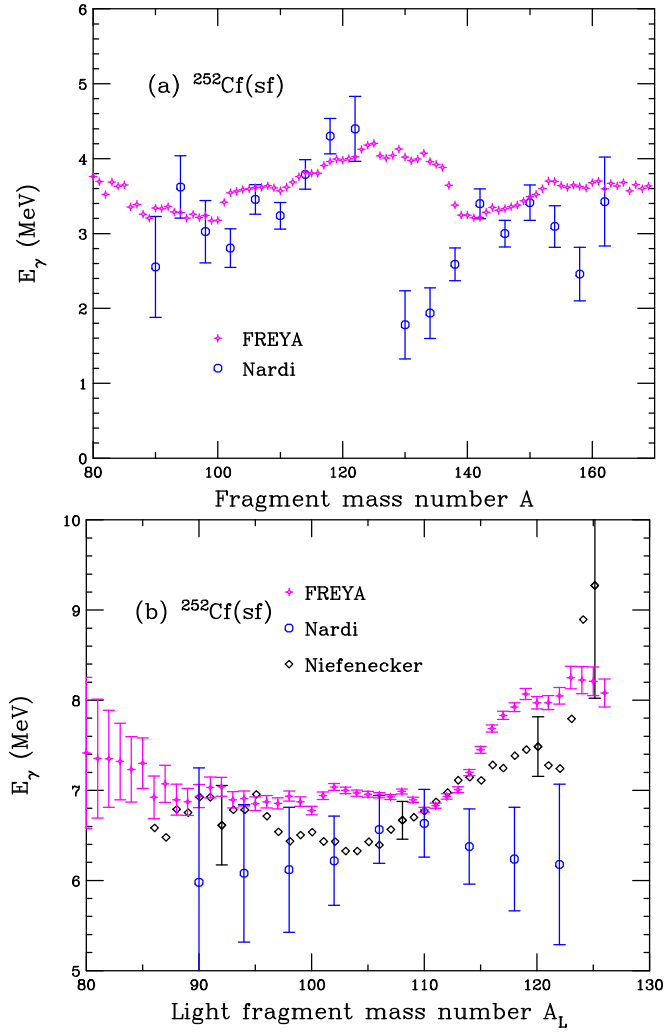

FIG. 19. For ^{252}Cf(sf), the calculated total photon energy E_γ as a function of the primary fragment mass number A (a) and the combined photon energy from both fragments as a function of the mass number of the light fragment A_L (b), compared to data from Nifenecker [26] (b) and from Nardi [27] (a) and (b). The calculation used one million events; the associated sampling errors are shown in (b).

Figure 20 compares the TKE dependencies obtained by Nifenecker [26] and Nardi [27] to the FREYA results. Again, representative uncertainties are shown for the Nifenecker data at several values of TKE (157, 166, 181, 196, and 208 MeV). Aside from the smallest values of TKE, TKE < 157 MeV, these data decrease linearly with TKE. This behavior is similar to the decrease seen for neutrons, ν(TKE), in other experiments. The Nardi data, on the other hand, exhibit a slower decrease that plateaus for TKE > 160 MeV. The overall average photon energy seems to be smaller for the Nardi measurement, as can also be observed through the comparison as a function of light fragment mass in Fig. 19(b). Note that

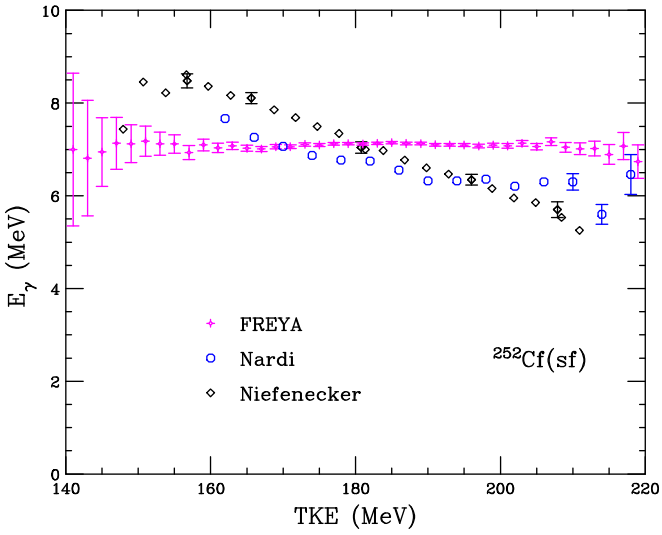

FIG. 20. For ^{252}Cf(sf), the calculated total photon energy as a function of total fragment kinetic energy is compared to data from Nifenecker [26] and Nardi [27].

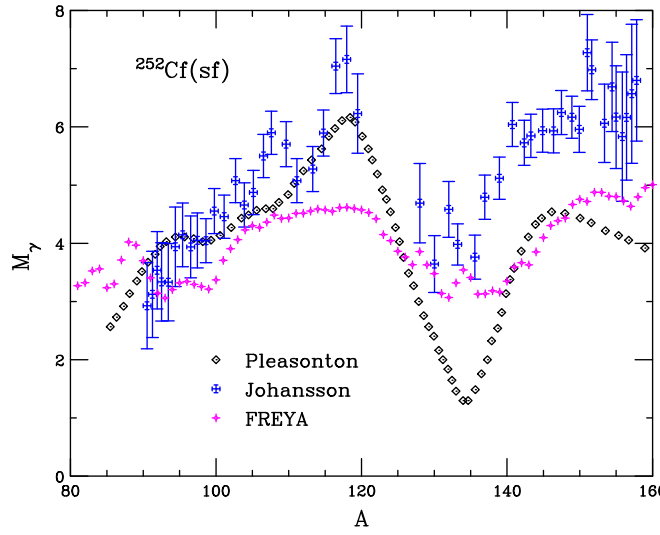

FIG. 21. The photon multiplicity as a function of fragment mass calculated for ^{252}Cf(sf) are compared to data from Pleasonton [28] and Johansson [29]. (Note that the method used by Johansson does not allow precise determination of the mass [29]).

the width of the TKE distribution is rather broad, allowing for significant photon emission up to TKE = 220 MeV.

The calculations suggest that, at least for ^{252}Cf(sf), E_γ is effectively independent of TKE. We have used $g_{\min} = 0.1$ MeV and $t_{\max} = 10$ ns in the FREYA calculations. As shown in the previous section, E_γ depends only weakly on $g_{\min}$, especially relative to the total multiplicity N_γ. It also shows a weaker dependence on $t_{\max}$ than N_γ; see Fig. 17.

Pleasonton *et al.* performed several experiments studying photon emission in thermal neutron-induced fission on ^{233,235}U and ^{239}Pu [31,32] as well as ^{252}Cf(sf) [28]. All four experiments were performed at Oak Ridge in the early 1970s. The setup included two surface barrier detectors to measure fragments and a sodium iodide detector to measure prompt fission photons ($t_{\max} = 5$ ns) with energies greater than 0.122 MeV. Data were taken in two different modes, a two-parameter mode to record only fragment masses and energies and a four-parameter mode in which time of flight was used to record the difference in arrival times between photons from the two fragments. A combined analysis of the data from the two- and four-parameter mode runs allowed separation of the photon yields into those from light and heavy fragments, yielding the photon energy and multiplicity as a function of fragment mass. The neutron-induced fission data used neutrons from the ORNL reactor while, for the Cf measurements, the apparatus remained in position but the neutron beam was turned off. The Pleasonton Cf data, shown in Fig. 21, are digitized from Ref. [28] where they were presented as a curve without uncertainties.

The data taken by Johansson in 1964 [29] used a ^{252}Cf source with two fragment detectors placed inside a thin walled, evacuated aluminum chamber. Photons were detected within 1 ns of emission using a sodium-iodide crystal. Photons from individual fragments were separated using a lead collimator: by alternating the position of the collimator, results were taken for each fragment and the results from the two collimator positions summed. From spectral data for different fragment masses, Fig. 8 of Ref. [29], it would appear that $g_{\min} \sim 0.2$ MeV for the measurement but no explicit photon energy cutoff is given. (Note that while the text of Ref. [29] refers to fission fragments, it is not clear how, or if, there has been a correction from the fission product. In addition, the mass and charge resolution of the experiment is rather poor so there is some uncertainty in the mass value.) While the photon multiplicity from the light fragment reported in this experiment is compatible with that of Pleasonton, the Pleasonton multiplicity is considerably lower for the heavy fragment. However, it is difficult to say how much the results differ without knowing the uncertainties in the Pleasonton data. If the energy cutoff is higher for Johansson than for Pleasonton, one might expect that the overall photon multiplicity would be lowered, similar to the FREYA results shown in Fig. 11.

We note that Johansson published a similar result a year later that was focused on delayed photons with emission times of 10–100 ns [33]. The delayed emission is more sensitive to long-lived isomers and thus to the transition lines in the RIPL database. There are prominent contributions to the delayed photon multiplicity at $A = 92$, 95, 110, 130, 134, and 148 which would fill in some of the dips in the prompt photon multiplicity, making the total multiplicity from the combined Johansson data sets closer to a sawtooth, as observed by John *et al.* [34].

The FREYA results are similar to but somewhat below the multiplicity of the light fragment as given by the two data sets. Also, while the calculations underestimate the Johansson data, they are in agreement with the Pleasonton results for $A > 140$. The FREYA results are furthest off from the Pleasonton data close to symmetry, $115 < A < 140$, where the uncertainties are likely large. While our results are not a fit to the average photon energy and multiplicity, our averages, $N_\gamma = 8.18$, $E_\gamma = 7.11$ MeV, and $E_\gamma/N_\gamma = 0.84$ MeV, are compatible

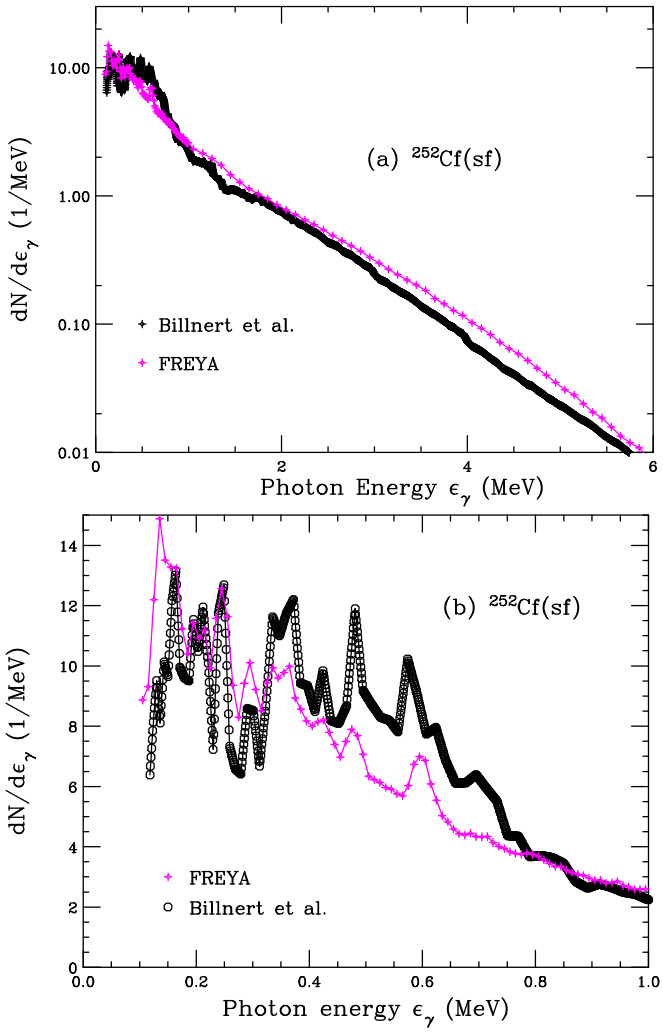

FIG. 22. The photon energy spectrum calculated for ^{252}Cf(sf) compared to data from Billnert *et al.* [18]. The total photon spectrum is shown in (a) while the spectrum for energies less than 1 MeV are shown in (b). The spectra are normalized to the fission photon multiplicity.

with those of Pleasonton [28]: $N_\gamma = 8.32 \pm 0.40$, $E_\gamma = 7.06 \pm 0.35$ MeV, and $E_\gamma/N_\gamma = 0.84 \pm 0.06$ MeV. We use the same values of $g_{\min}$ and $t_{\max}$ as Pleasonton, $g_{\min} = 0.12$ MeV and $t_{\max} = 5$ ns. Since we do not have the exact $g_{\min}$ for Johansson, we use that of Pleasonton for the comparison.

Figure 22 shows the prompt fission photon spectrum for ^{252}Cf(sf) measured by Billnert *et al.* [18]. They have embarked on a campaign to make modern measurements of photon decay heat generated during fission, in particular for isotopes relevant for reactors. To do this, they first made measurements of the ^{252}Cf(sf) photon spectrum. They used two different detectors: lanthanum bromide, for timing and energy resolution, and cesium bromide, because of the absence of intrinsic photon activity in this material. The energy and timing resolution for these detector materials is better than that of the sodium iodide-based detectors used in previous measurements. They were able to reduce the uncertainties of their measurement considerably relative to previous results [18]: $N_\gamma = 8.30 \pm 0.08$; $E_\gamma = 6.64 \pm 0.08$ MeV; and $E_\gamma/N_\gamma = 0.80 \pm 0.01$ MeV, including relative to that of Pleasonton, mentioned above. The results for the two different detector materials agree. In this case, we use the same energy cutoff, $g_{\min} = 0.1$ MeV, and time window, $t_{\max} = 1.5$ ns, in the FREYA calculations as in the measurement.

The calculated photon spectrum is normalized to the total calculated multiplicity, $N_\gamma = 8.37$, obtained for the $g_{\min}$ and $t_{\max}$ used by Billnert *et al.* The overall agreement, shown in Fig. 22(a), is very good. (Note that the uncertainties on the measurement, shown for the lanthanum bromide detectors, are not included in the plot. With these included, the apparent agreement would improve. Incorporating the GDR into FREYA provides the harder spectrum for high-energy continuum emission, as exhibited in the data.

Note that our average calculated photon energy, $\langle E_\gamma \rangle = 7.09$ MeV, is higher that that measured by Billnert *et al*. Thus even though our photon multiplicity is within the uncertainties of the data, the higher photon energy from FREYA results in a higher average energy per photon, $E_\gamma/N_\gamma = 0.85$ MeV.

Figure 22(b) focuses on the low-energy part of the photon spectrum, $E_\gamma < 1$ MeV, where the RIPL-3 transitions play the most important role. While the magnitudes of the peaks from the data and from FREYA do not precisely match, the locations match quite well. The differences in the strength of the peaks are likely due to the rather rough manner of substituting branching ratios that are not included in the RIPL-3 tabulation. We note that without our model refinements, the calculations would underestimate the photon spectrum at high energy and would not exhibit any structure at low photon energies.

Finally, in Fig. 23, we compare FREYA to measured photon multiplicity distributions.

The prompt photon energy and the prompt photon multiplicity distribution were measured [19] with the highly segmented 4π photon calorimeter of the Detector for Advanced Neutron Capture Experiments (DANCE) [37] combined with a compact gas-filled parallel-plate avalanche counter [38]. The energy and multiplicity distributions were unfolded to produce the first experimental measurement of $P_\gamma(N)$ in spontaneous fission [19]. The unfolded multiplicity distribution makes it possible to study the moments of the photon multiplicity distribution, similar to studies making use of factorial moments of the neutron multiplicity distribution.

The distribution from DANCE, shown in Fig. 23(a), has $\langle N_\gamma \rangle = 8.14 \pm 0.40$ for $g_{\min} = 0.14$ MeV. While the average multiplicity calculated with FREYA for this same $g_{\min}$ is 7.94, within the uncertainty of the data, the FREYA distribution is significantly narrower than the data (the dispersion of the calculated distribution is 2.81, while that of the data is 3.35). The more recent results of Oberstedt *et al.* [35] is in rather good agreement with the DANCE data. The earlier evaluation by Valentine [36] is somewhat narrower than the more recent measurement, in better agreement with FREYA.

We note that although the introduction of thermal fluctuations in the excitation energy (through the parameter c_T) may affect the moments of the neutron multiplicity distribution, these fluctuations do not affect the width of the photon multiplicity distribution because a significant fraction of the

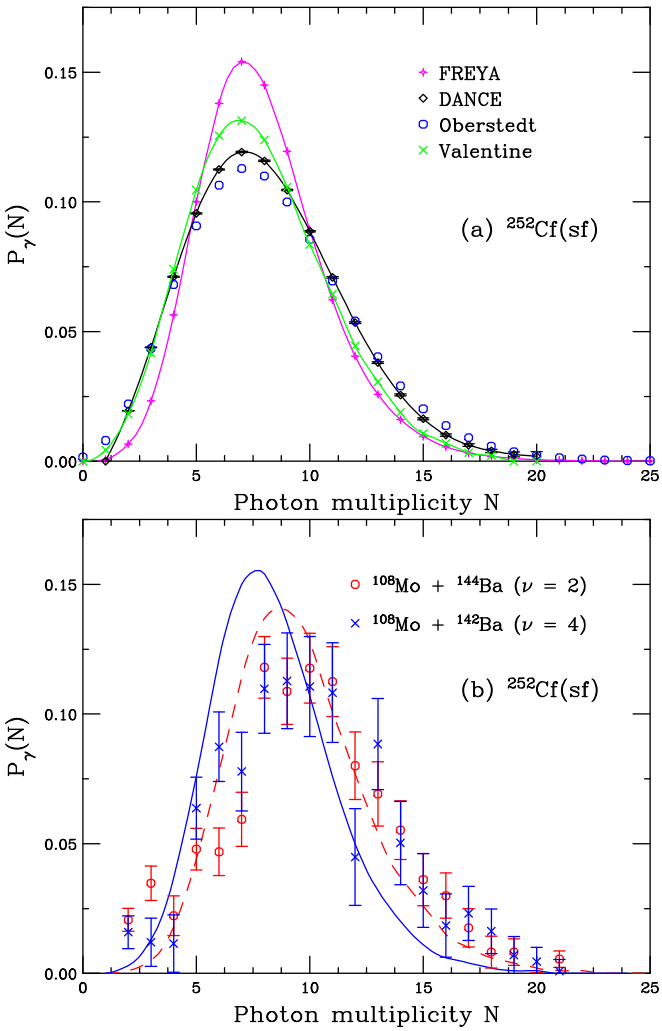

FIG. 23. (a) The photon multiplicity distribution $P(N_\gamma)$ calculated for ^{252}Cf(sf) is compared to data from DANCE [19] as well as data from Oberstedt *et al.* [35] and the Valentine evaluation [36]. (b) The LiBerACE [30] photon multiplicity distributions resulting from two and four neutrons emitted compared to the FREYA results for the same quantities.

excitation energy has already been carried away through neutron evaporation before photon emission begins. However, the photon multiplicity distribution is affected somewhat by the degree of angular momentum carried away during the statistical part of the photon emission cascade.

The Livermore-Berkeley Array for Collaborative Experiments (LiBerACE) used ^{252}Cf(sf) to study photon multiplicity relative to neutron emission [30]. They surrounded the ^{252}Cf source with high-purity germanium detectors enclosed in bismuth-germanate detectors. The geometry of the detector array provided good solid angle coverage. Room background, as well as photons from cosmic rays, were subtracted by counting photons with no source present.

The LiBerACE Collaboration exploited the observation of discrete energy photons coming from known transitions in identified fission products, after neutron emission, to study neutron-photon correlations. They hoped to determine whether neutron and photon emission was positively or negative correlated. Energy- and momentum-conserving calculations of neutron and photon emission in fission [6,39], such as FREYA, predicts an anticorrelation between photons and neutrons, i.e., the average photon multiplicity would decrease with increasing neutron multiplicity. On the other hand, Nifenecker *et al.* [26] suggested that there was a positive correlation between neutron multiplicity and photon energy.

They focused on two pairs of deformed even-even product nuclei, ^{106}Mo/^{144}Ba and ^{106}Mo/^{142}Ba, which are associated with the emission of two or four neutrons, respectively. They compared the photon multiplicity distributions from these product pairs. If the emission is anticorrelated, a backward shift in the centroid of the photon multiplicity distribution should be observed when comparing the first pair with the second pair, i.e., comparing two-neutron emission with four-neutron emission, and vice versa if there is a positive correlation. As seen in Fig. 23(b), there is no observable difference in the location of the centroid for the selected Mo/Ba ratios within their significant statistical uncertainties, suggesting the absence of a correlation between neutron and photon emission.

FREYA results for the photon multiplicity distribution with two and four neutrons emitted from all fragment pairs are also shown in Fig. 23(b). The calculations use the experimental $g_{\rm min}$ value of 0.1 MeV and the time window with $t_{\rm max} = 2\,\mu$s. There is a clear shift in the calculations to lower photon multiplicity for the emission of four neutrons. We note, however, that the FREYA results shown here are based on all fragment pairs, not just the two Mo/Ba pairs employed in the measurement.

B. ^{235}U($n_{\rm th}$,f)

Here we compare the FREYA results to the Pleasonton measurements of photon energy and multiplicity as a function of fragment mass and total kinetic energy [31] as well as the multiplicity measurement as a function of fragment mass by Albinsson [40]. The recent spectral measurement by Oberstedt *et al.* [41] is also included. We have not modified c_S for neutron-induced fission but use the value determined from the preliminary fit to the ^{252}Cf(sf) data, $c_S = 0.87$. The parameters x, c_T, and dTKE are tuned to ^{235}U($n_{\rm th}$,f) neutron data employing $c_S = 0.87$ while the value of e_0 is assumed to be the same for all fissioning nuclei, both spontaneous and neutron induced.

The detector setup for the Pleasonton experiment was the same as for the ^{252}Cf(sf) measurement described in the previous section except that, for this measurement, as well as for other measurements, shown in the Appendix for ^{233}U($n_{\rm th}$,f) and ^{239}Pu($n_{\rm th}$,f) [32], the data were taken with thermal neutrons from the Oak Ridge National Laboratory research reactor. The target, in this case a 99.44% pure thin deposit of $^{235}U_3O_8$ on a backing, was placed at a 45° angle to the neutrons from the reactor. The fragment detectors were placed at 45° angles on either side of the target, 90° away from the neutron direction and in line with the sodium iodide crystal to measure photons from fission events. As described previously, the experiment was run in two different modes, the two-parameter mode to study fragment masses and kinetic energies and the four-parameter mode for timing to separate

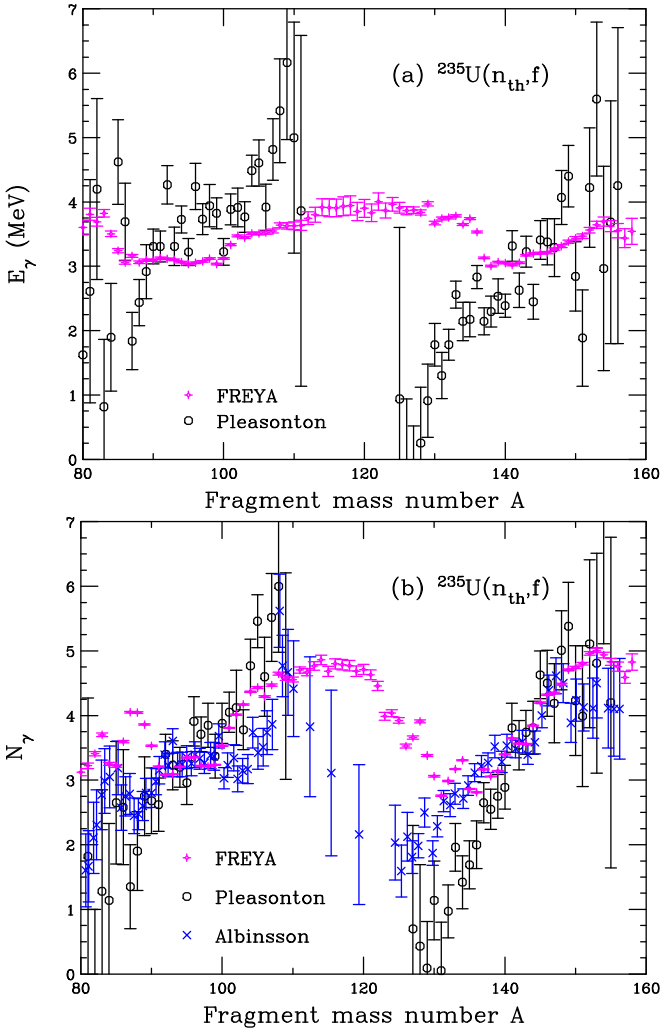

FIG. 24. The total photon energy (a) and the photon multiplicity (b) as a function of fragment mass calculated for ^{235}U(n_{th},f) are compared to data from Pleasonton [31] (a) and (b), and data from Albinsson [40] (b).

the photons from the light and heavy fragments. They collected 306 000 events in the four-parameter mode and 852 000 events in the two-parameter mode. In such cases, the statistics from the four-parameter mode sets the level of statistics for the data.

The FREYA results are compared to the Pleasonton data on photon energy as a function of fragment mass in Fig. 24(a). The uncertainties in the data are rather large and there is considerable point-to-point scatter. The trend of the data appears to be an approximately linear increase in E_γ with A in both the light and heavy fragment regions. The region near symmetry, $110 < A < 125$, is effectively devoid of data due to the small fragment yields in this region. The tails of the fragment distributions, $A < 90$ and $A > 145$, also having small fragment yields, exhibit large uncertainties in E_γ as well. Thus the data are also effectively consistent with being independent of A within one standard deviation. The FREYA calculations are nearly independent of A and are also within one standard deviation of the data for $A < 110$ and $A > 130$.

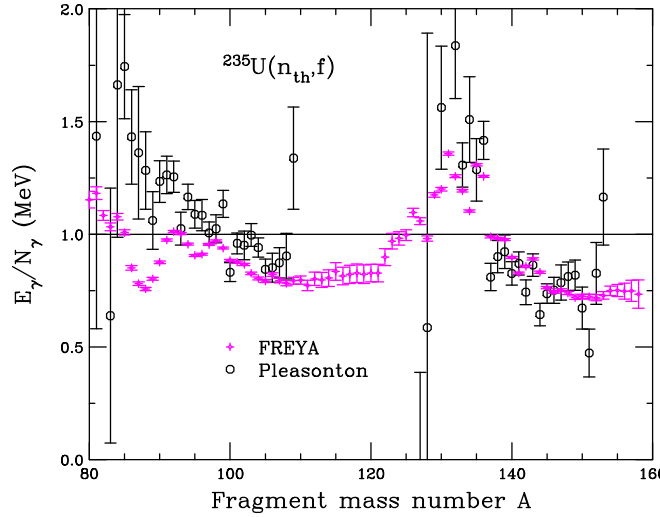

FIG. 25. The energy per photon as a function of fragment mass calculated for ^{235}U(n_{th},f) is compared to data from Pleasonton [31].

The dependence of E_γ on A in FREYA has not changed significantly with the model improvements.

Note that the statistical uncertainties on the calculation are shown as well. Since our results are based on one million events with several photons emitted per event, the FREYA results have significantly higher statistics than the four-parameter mode of the experiment that recorded the photon data. The largest statistical uncertainties in the calculation are in the symmetric fission region.

In addition to the Pleasonton data on photon multiplicity, results from Albinsson and Lindow [40] are also shown in Fig. 24(b). The measurement by Albinsson and Lindow used an experimental setup similar to Pleasonton, with a collimated neutron beam from the Studsvik R2 reactor. However, similar to the Johansson measurement [29], they used a movable

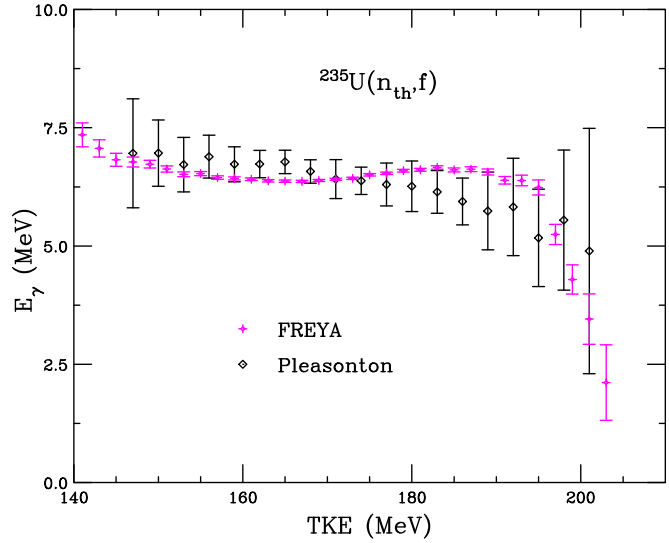

FIG. 26. The total photon energy as a function of total fragment kinetic energy calculated for ^{235}U(n_{th},f) is compared to data from Pleasonton [31].

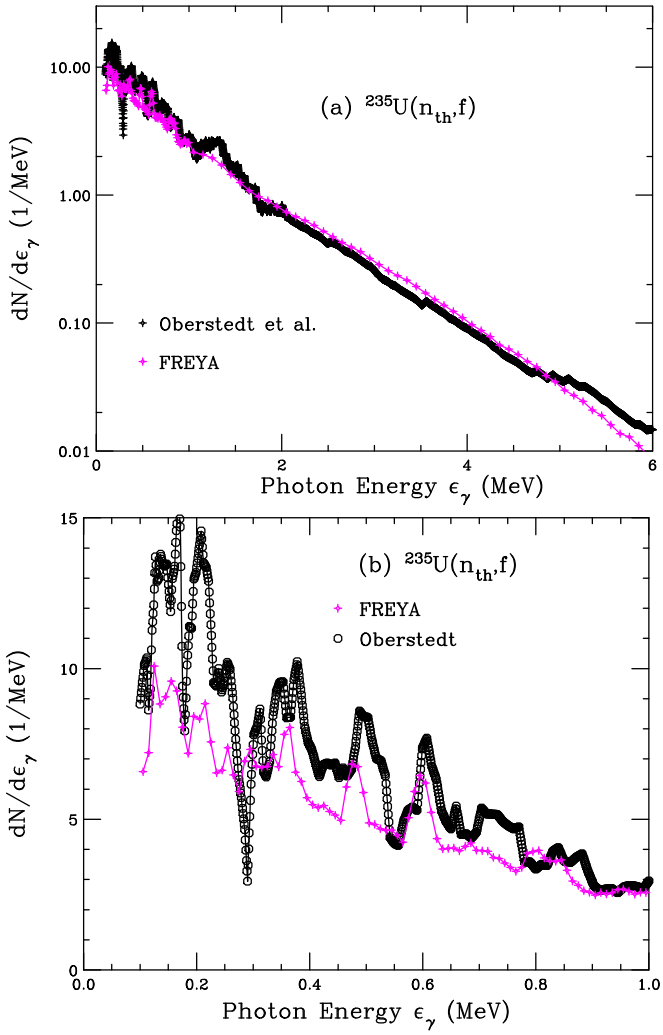

FIG. 27. The photon energy spectrum calculated for ^{235}U($n_{\rm th}$,f) compared to data from Oberstedt *et al.* [41]. The total photon spectrum is shown in (a) while the spectrum for energies less than 1 MeV is shown in (b). The spectra are normalized to the fission photon multiplicity.

lead collimator to track fragments from individual fragments and for timing purposes. Their results are similar to those from Pleasonton although the multiplicity trends lower for Albinsson for $A > 100$ and higher for $125 < A < 140$. We note that the calculation shown is done using the values of $g_{\rm min}$ and $t_{\rm max}$ suitable for the Pleasonton experiment. These values are, however, compatible with those used in the measurement by Albinsson and Lindow. Given the large uncertainties in the two data sets, the agreement with the FREYA calculation is good. Comparison with Fig. 2(b) shows that the model refinements makes the shape of $N_\gamma(A)$ more compatible with the data.

Figure 25 compares the energy per photon from Pleasonton with FREYA. Overall, the agreement is quite good. The FREYA calculation reproduces the peak in E_γ/N_γ near $A \approx 130$. We note that only including the model improvements produces the peak in E_γ/N_γ at $A \sim 130$; see Fig. 3. While there are some differences for $A < 90$, due to a small enhancement in the

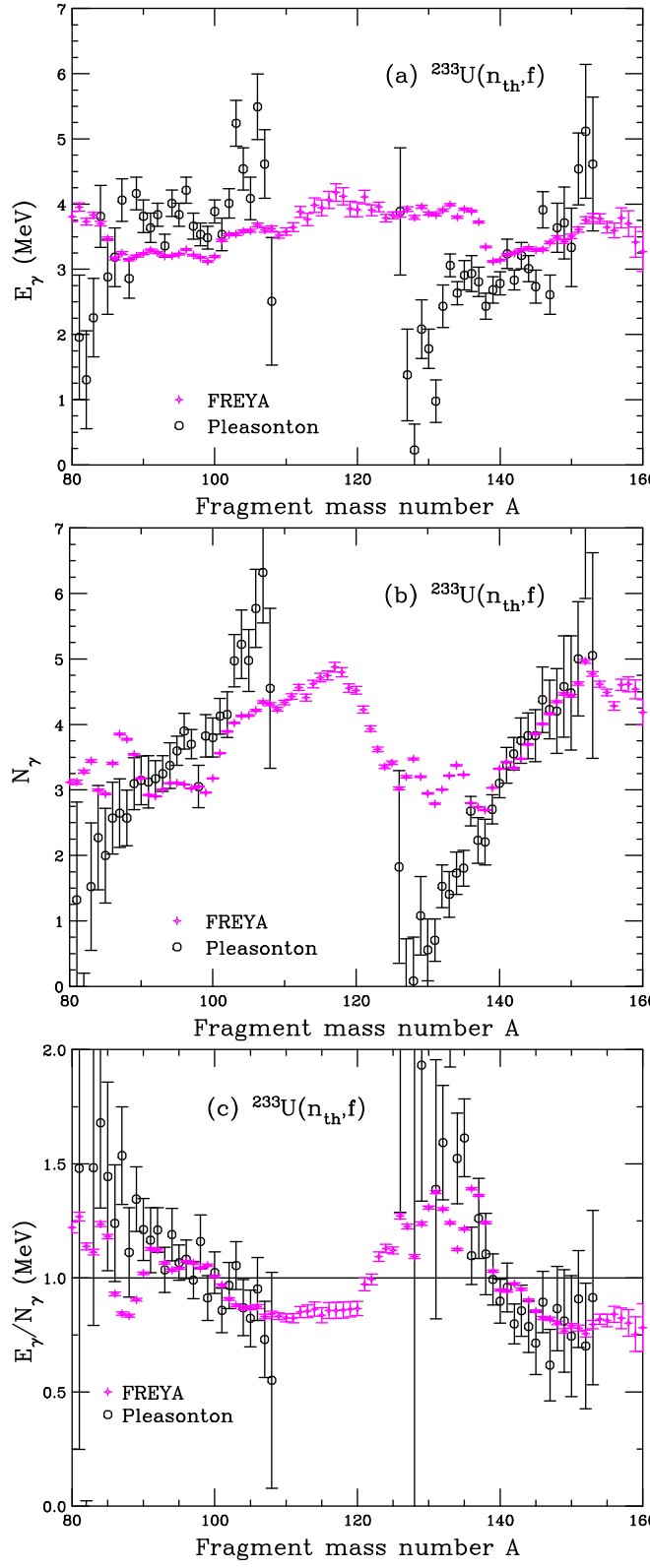

FIG. 28. The total photon energy (a), the photon multiplicity (b), and the energy per photon (c) as functions of fragment mass number calculated for ^{233}U($n_{\rm th}$,f) are compared to data from Pleasonton [32].

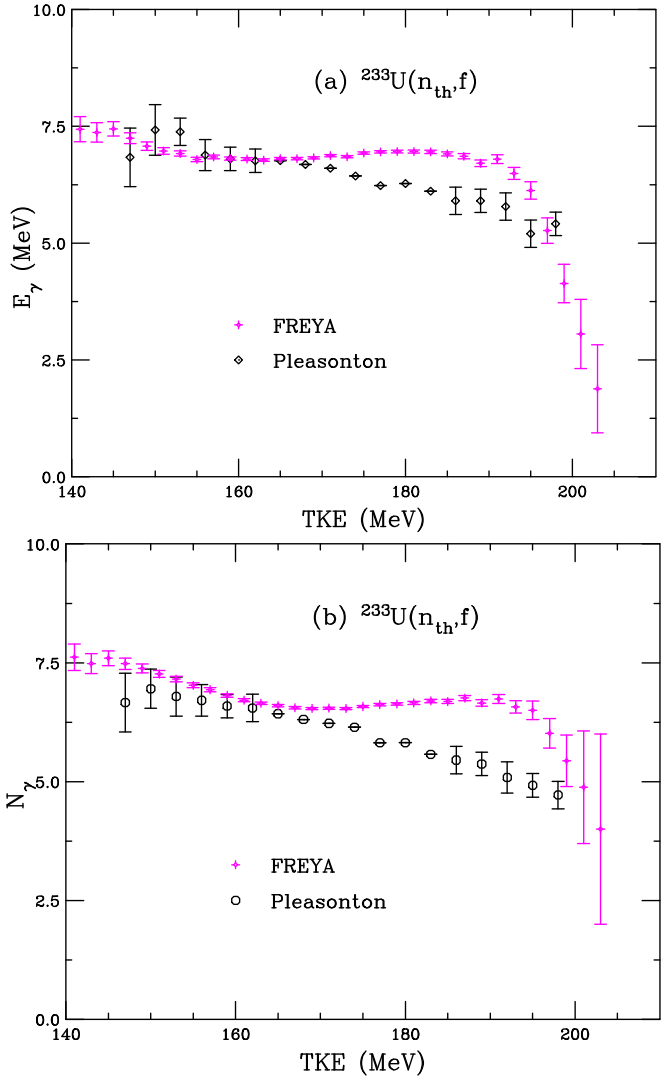

FIG. 29. The total photon energy as a function of total fragment kinetic energy calculated for ^{233}U($n_{\rm th}$,f) is compared to data from Pleasonton [32].

photon multiplicity for $A \approx 88$, producing a dip in E_γ/N_γ at this value of A, the uncertainties are large enough for the two to still be reasonably compatible. The results for the mean photon multiplicity, total photon energy, and energy per photon, $N_\gamma = 6.82$; $E_\gamma = 6.47$ MeV; and $E_\gamma/N_\gamma = 0.95$ MeV, agree well with those of Pleasonton [31], $N_\gamma = 6.51 \pm 0.30$; $E_\gamma = 6.43 \pm 0.30$ MeV; and $E_\gamma/N_\gamma = 0.99 \pm 0.07$ MeV, and are also compatible with the earlier measurement of Verbinski *et al.* [42].

Our results are also compared to the photon energy as a function of total kinetic energy in Fig. 26. Contrary to the ^{252}Cf(sf) calculation shown in Fig. 20, the FREYA calculation for ^{235}U($n_{\rm th}$,f) is not independent of TKE. Although the curvature appears to be somewhat different than that of the data, the results agree within the uncertainties. Note also the falloff of the calculation for TKE > 190 MeV, due to the narrower TKE distribution for ^{235}U($n_{\rm th}$,f) relative to ^{252}Cf(sf). In this case the upper bound of TKE is 205 MeV.

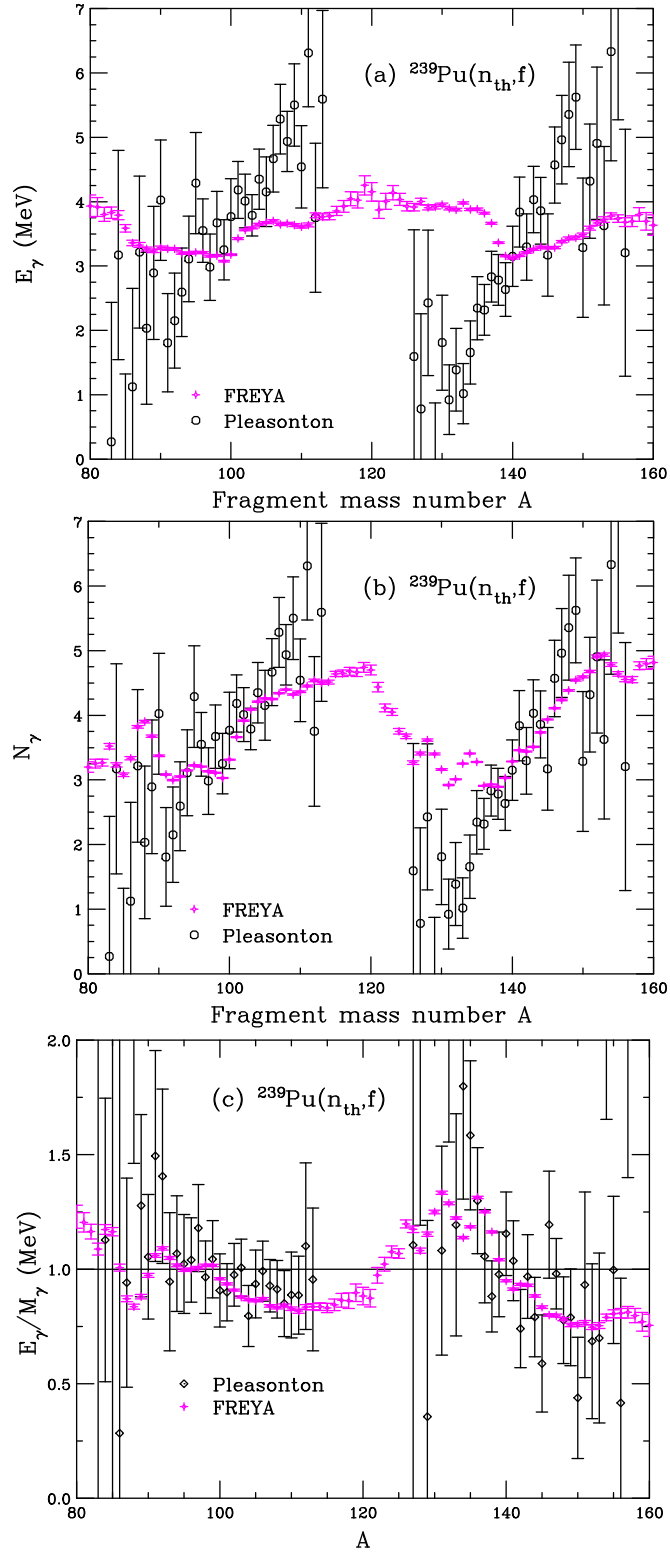

FIG. 30. The total photon energy (a) and the photon multiplicity (b) as a function of fragment mass calculated for ^{239}Pu($n_{\rm th}$,f) are compared to data from Pleasonton [32].

Finally, we compare our calculated prompt fission photon spectrum to the results of Oberstedt *et al.* [41]. This measurement is a continuation of the work of Billnert *et al.* [18] for ^{252}Cf(sf) shown in Fig. 22 with the same detectors and

values of $g_{\min}$ and $t_{\max}$ as in that work. In this case the measured high-energy slope of the photon energy spectrum is in good agreement with the FREYA calculation, even without including the experimental uncertainties. Without our model refinements, the calculations would underestimate the photon spectrum at high energy and would not exhibit any structure at low photon energies. The peaks observed in the low-energy part of the photon spectrum, shown in Fig. 27(b), also agree well with the FREYA calculation. Oberstedt *et al.* measured $N_\gamma = 8.19 \pm 0.11$, $E_\gamma = 6.92 \pm 0.09$ MeV, and $E_\gamma/N_\gamma = 0.85 \pm 0.02$ MeV, while, for the same cutoffs, we find $N_\gamma = 6.93$, $E_\gamma = 6.48$ MeV, and $E_\gamma/N_\gamma = 0.93$ MeV. The somewhat lower values of $g_{\min}$ and $t_{\max}$ for this experiment results in the slightly higher N_γ calculated here than the calculation for the Pleasonton data.

We note that, overall, we have achieved rather good agreement with the photon data, despite not having made any global parameter analyses to extract c_S specifically for ^{235}U($n_{\rm th}$,f).

VII. CONCLUSIONS

We have shown that the inclusion of the GDR form factor and the RIPL-3 transitions into FREYA has improved the photon emission process, resulting in better agreement with photon observables as compared to our previous work [2]. In particular, there is significant improvement for the photon energy spectrum and the A dependence of the energy per photon. However, there is still room for further improvements, particularly with regard to the shape of the photon multiplicity distribution. We will return to this in future work.

We have also studied the sensitivity of our results to the degree of rotation imparted to the fragments during scission by means of the scale factor c_S controlling the ratio between the fragment spin temperature and the scission temperature. Furthermore, we have illustrated how the photon energy and the photon multiplicity measured by different experiments depend on detector characteristics such as the minimum energy of the detected photons, $g_{\min}$, and the time window over which the measurement is made, $t_{\max}$.

The calculations were made with a value of c_S optimized for ^{252}Cf(sf). (Note that, as mentioned in Sec. VI B, the parameters x, c_T, and dTKE were tuned to the neutron observables for the fixed value $c_S = 0.87$.) Even so, the agreement of our results with photon measurements in neutron-induced fission is also quite good. Further improvement can likely be obtained by performing a global parameter optimization including c_S, a subject of future work.

We expect that the quality of the agreement of the FREYA calculations with experimental data will continue to improve as further model refinements are made and more measurements become available for both optimization and predictive capability, for example, fission induced by (d,p) scattering; see Ref. [43].

ACKNOWLEDGMENTS

We thank P. Talou for helpful discussions. This work performed under the auspices of the U.S. Department of Energy by Lawrence Livermore National Laboratory under Contract No. DE-AC52-07NA27344 (R.V.) and by Lawrence Berkeley National Laboratory under Contract No. DE-AC02-05CH11231 (J.R.). The authors wish to acknowledge the Office of Defense Nuclear Nonproliferation Research and Development in the U.S. Department of Energy's National Nuclear Security Administration for their support.

APPENDIX: ^{233}U($n_{\rm th}$,f) AND ^{239}Pu($n_{\rm th}$,f)

In this Appendix we compare our results with those measured by Pleasonton for ^{233}U($n_{\rm th}$,f) and ^{239}Pu($n_{\rm th}$,f) [32]. The experimental setup is the same as for the previously described Pleasonton measurements of ^{235}U($n_{\rm th}$,f). The values of $g_{\min}$ and $t_{\max}$ were the same as those for the measurement. In both cases, $c_S = 0.87$, obtained for ^{252}Cf(sf), is used in the calculations. The values of x, c_T, and dTKE were fixed to neutron observables. We are working toward global analyses, including fitting c_S to the data, in the future. Nonetheless, we

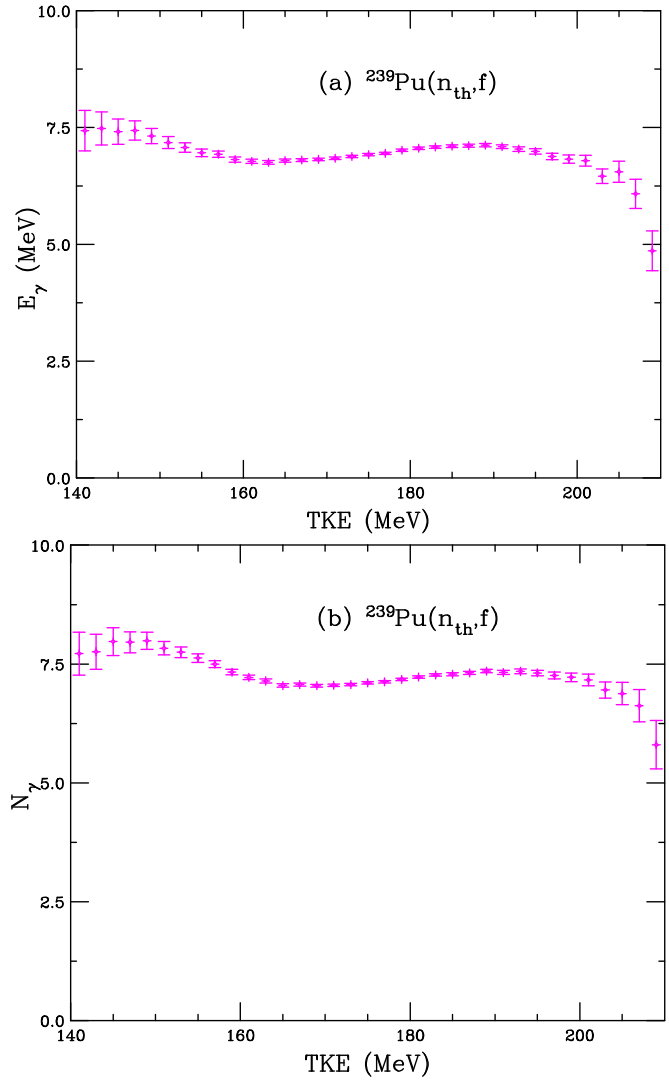

FIG. 31. The total photon energy as a function of total fragment kinetic energy calculated for ^{239}Pu($n_{\rm th}$,f).

can already check whether or not the calculated trends are reasonable.

1. ^{233}U(n_{th},f)

For ^{233}U(n_{th},f), a 99.9% pure $^{233}U_3O_8$ target was placed on a carbon film; 920 000 events were collected in the two-parameter mode and 350 000 events in the four-parameter mode.

The results for the total photon energy, photon multiplicity, and energy per photon are shown in Fig. 28. The trends of the calculations and the data are similar. Here the total photon energy appears to have a somewhat weaker dependence on fragment mass A than did the ^{235}U measurement in Fig. 24(a).

The measured average multiplicities and energies are $\langle N_\gamma \rangle = 6.31 \pm 0.30$; $\langle E_\gamma \rangle = 6.69 \pm 0.30$ MeV; and $\langle E_\gamma / N_\gamma \rangle = 1.06 \pm 0.07$ MeV. Our calculations give $\langle N_\gamma \rangle = 6.66$; $\langle E_\gamma \rangle = 6.87$ MeV; and $\langle E_\gamma / N_\gamma \rangle = 1.03$ MeV, in very good overall agreement with the data.

The total photon energy and multiplicity are shown as functions of the total fragment kinetic energy in Fig. 29. The calculated shape is similar to that obtained for ^{235}U. Here, however, the measured uncertainties shown are smaller than those for ^{235}U, giving a clearer suggestion of small decrease in both E_γ and N_γ with TKE. The calculations agree with the data for TKE < 170 MeV.

2. ^{239}Pu(n_{th},f)

For ^{239}Pu(n_{th},f), a 99.11% pure $^{239}PuO_2$ target was deposited on a carbon film; 641 000 events were collected in the two-parameter mode and 209 000 events in the four-parameter mode.

The results for the total photon energy, photon multiplicity, and energy per photon are shown in Fig. 30. The trends of the calculations and the data are similar and the agreement is generally good. However, the low statistics of this data set make it difficult to conclude anything substantial.

The measured average multiplicities and energies are $\langle N_\gamma \rangle = 6.88 \pm 0.35$; $\langle E_\gamma \rangle = 6.73 \pm 0.35$ MeV; and $\langle E_\gamma / N_\gamma \rangle = 0.98 \pm 0.07$ MeV. Our calculations give $\langle N_\gamma \rangle = 7.19$; $\langle E_\gamma \rangle = 6.95$ MeV; and $\langle E_\gamma / N_\gamma \rangle = 0.98$ MeV. While our calculated averages are somewhat higher than the data, they are still within the uncertainties.

For completeness, the photon energy and multiplicity are shown as functions of TKE in Fig. 31. The results are similar to those for the other neutron-induced fission calculations shown above. No data were available for comparison for this case. Note that the calculations extend to higher values of TKE than for ^{233}U(n_{th},f) and ^{235}U(n_{th},f) because the tail of the TKE distribution extends to higher TKE for ^{239}Pu(n_{th},f), up to 215 MeV.

[1] R. Vogt, J. Randrup, D. A. Brown, M. A. Descalle, and W. E. Ormand, Event-by-event evaluation of the prompt fission neutron spectrum from ^{239}Pu(n, f), Phys. Rev. C **85**, 024608 (2012).

[2] R. Vogt and J. Randrup, Event-by-event study of photon observables in spontaneous and thermal fission, Phys. Rev. C **87**, 044602 (2013).

[3] J. Verbeke, R. Vogt, and J. Randrup, Fission Reaction Event Yield Algorithm, FREYA–For event-by-event simulation of fission, Comput. Phys. Commun. **191**, 178 (2015).

[4] J. M. Verbeke, R. Vogt, and J. Randrup, Comput. Phys. Commun. **222**, 263 (2018).

[5] R. Vogt, A. Nicholson, J. Randrup, I. Gauld, and S. Croft, Uncertainty Quantification with the Event-by-Event Fission Model FREYA, in *Proceedings of the First ANS Advances in Nuclear Nonproliferation Technology and Policy Conference*, Santa Fe, NM, 2016, LLNL-CONF-690741.

[6] R. Vogt and J. Randrup, Event-by-event study of neutron observables in spontaneous and thermal fission, Phys. Rev. C **84**, 044621 (2011).

[7] J. Randrup and R. Vogt, Refined treatment of angular momentum in the event-by-event fission model FREYA, Phys. Rev. C **89**, 044601 (2014).

[8] R. Vogt and J. Randrup, Neutron angular correlations in spontaneous and neutron-induced fission, Phys. Rev. C **90**, 064623 (2014).

[9] B. L. Berman and S. C. Fultz, Measurements of the giant dipole resonance with monoenergetic photons, Rev. Mod. Phys. **47**, 713 (1975).

[10] R. Capote *et al.*, RIPL – Reference input parameter library for calculations of nuclear reactions and nuclear data evaluations, Nucl. Data Sheets **110**, 3107 (2009).

[11] O. Litaize, O. Serot and L. Berge, Fission modeling with FIFRELIN, Eur. Phys. J. A **51**, 177 (2015).

[12] P. Talou, T. Kawano, and I. Stetcu, CGMF, Version 1.0, Tech. Rep. LA-CC-13-063, Los Alamos National Laboratory, 2013.

[13] K. H. Schmidt, B. Jurado, C. Amouroux, and C. Schmitt, General Description of Fission Observables: GEF Model Code, Nucl. Data Sheets **131**, 107 (2016).

[14] W. Mannhart, The high energy portion of the Cf-252 neutron spectrum deduced from integral experiments, in *Proceedings of an Advisory Group Meeting on Properties of Neutron Sources (IAEA-TECDOC-410)*, Vienna (IAEA, Vienna, 1987), pp. 194–201.

[15] J. W. Boldeman and M. G. Hines, Prompt neutron emission probabilities following spontaneous and thermal neutron fission, Nucl. Sci. Eng. **91**, 114 (1985).

[16] V. N. Dushin *et al.*, Facility for neutron multiplicity measurements in fission, Nucl. Instrum. Methods, Phys. Res. A **516**, 539 (2004).

[17] C. Budtz-Jørgensen and H.-H. Knitter, Simultaneous investigation of fission fragments and neutrons in ^{252}Cf(sf), Nucl. Phys. A **490**, 307 (1988).

[18] R. Billnert, F.-J. Hambsch, A. Oberstedt, and S. Oberstedt, New prompt spectral γ-ray data from the reaction ^{252}Cf(sf) and its implication on present evaluated nuclear data files, Phys. Rev. C **87**, 024601 (2013).

[19] A. Chyzh, C. Y. Wu, E. Kwan, R. A. Henderson, J. M. Gostic, T. A. Bredeweg, R. C. Haight, A. C. Hayes-Sterbenz, M. Jandel, J. M. O'Donnell, and J. L. Ullmann, Evidence for the stochastic aspect of prompt γ emission in spontaneous fission, Phys. Rev. C **85**, 021601(R) (2012).

[20] I. Ahmad and W. R. Phillips, Rep. Prog. Phys. **58**, 1415 (1995).

[21] P. Talou, T. Kawano, I. Stetcu, J. P. Lestone, E. McKigney, and M. B. Chadwick, Late-time emission of prompt fission γ rays, Phys. Rev. C **94**, 064613 (2016).
[22] A. Göök, F.-J. Hambsch, and M. Vidali, Prompt neutron multiplicity in correlation with fragments from spontaneous fission, Phys. Rev. C **90**, 064611 (2014).
[23] P. Talou, B. Becker, T. Kawano, M. B. Chadwick, and Y. Danon, Advanced Monte Carlo modeling of prompt fission neutrons for thermal and fast neutron-induced fission reactions on ^{239}Pu, Phys. Rev. C **83**, 064612 (2011).
[24] B. Becker, P. Talou, T. Kawano, Y. Danon, and I. Stetcu, Monte Carlo Hauser-Feshbach predictions of prompt fission γ-rays: Application to $n_{\rm th} + ^{235}$U, $n_{\rm th} + ^{239}$Pu, and ^{252}Cf(sf), Phys. Rev. C **87**, 014617 (2013).
[25] I. Stetcu, P. Talou, T. Kawano, and M. Jandel, Properties of prompt-fission γ-rays, Phys. Rev. C **90**, 024617 (2014).
[26] H. Nifenecker, C. Signarbieux, M. Ribrag, J. Poitou, and J. Matuszek, Gamma-neutron competition in the de-excitation mechanism of the fission fragments of ^{252}Cf, Nucl. Phys. A **189**, 285 (1972).
[27] E. Nardi, A. Gavron, and Z. Fraenkel, Total energy associated with prompt γ-ray emission in the spontaneous fission of Cf-252, Phys. Rev. C **8**, 2293 (1973).
[28] F. Pleasonton, R. L. Ferguson, and H. W. Schmitt, Prompt Gamma Rays Emitted in the Thermal Neutron-Induced Fission of ^{233}U, ^{235}U, and ^{239}Pu and the Spontaneous Fission of ^{252}Cf, ORNL Report No. 4844, 1972, pp. 109–112.
[29] S. A. E. Johansson, Gamma de-excitation of fission fragments: (1) Prompt radiation, Nucl. Phys. **60**, 378 (1964).
[30] D. L. Bleuel *et al.*, Gamma-ray multiplicity measurement of the spontaneous fission of ^{252}Cf in a segmented HPGe/BGO detector array, Nucl. Instrum. Methods Phys. Res. A **624**, 691 (2010).
[31] F. Pleasonton, R. L. Ferguson, and H. W. Schmitt, Prompt gamma rays emitted in the thermal-neutron-induced fission of ^{235}U, Phys. Rev. C **6**, 1023 (1972).
[32] F. Pleasonton, Prompt γ-rays emitted in the thermal-neutron induced fissio of ^{233}U and ^{239}Pu, Nucl. Phys. A **213**, 413 (1973).
[33] S. A. E. Johansson, Gamma de-excitation of fission fragments: (2) Delayed radiation, Nucl. Phys. **64**, 147 (1965).
[34] W. John, J. J. Wesolowski, and F. Guy, Mass dependent structure in the fission γ-ray yields from ^{252}Cf, Phys. Lett. B **30**, 340 (1969).
[35] A. Oberstedt, R. Billnert, F.-J. Hambsch, and S. Oberstedt, Impact of low-energy photons on the characteristics of prompt fission γ-ray spectra, Phys. Rev. C **92**, 014618 (2015).
[36] T. E. Valentine, Evaluation of prompt fission gamma rays for use in simulating nuclear safeguard measurements, Ann. Nucl. Energy **28**, 191 (2001).
[37] M. Heil *et al.*, A 4π BaF_2 detector for (n, g) cross section measurements at a spallation neutron source, Nucl. Instrum. Methods Phys. Res. A **459**, 229 (2001).
[38] C. Y. Wu *et al.*, A compact gass-filled avalanche counter for DANCE, Nucl. Instrum. Methods Phys. Res. A **694**, 78 (2012).
[39] S. Lemaire, P. Talou, T. Kawano, M. B. Chadwick, and D. G. Madland, Monte Carlo approach to sequential γ-ray emission from fission fragments, Phys. Rev. C **73**, 014602 (2006).
[40] H. Albinsson and L. Lindow, Prompt Gamma Radiation from Fragments in the Thermal Fission of ^{235}U, Atomenergie Studavik, Sweden, Report No. AE-398, 1970.
[41] A. Oberstedt, T. Belgya, R. Billnert, R. Borcea, T. Bryś, W. Geerts, A. Göök, F.-J. Hambsch, Z. Kis, T. Martinez, S. Oberstedt, L. Szentmiklosi, K. Takàcs, and M. Vidali, Improved values for the characteristics of prompt-fission γ-ray spectra from the reaction ^{235}U($n_{\rm th}$, f), Phys. Rev. C **87**, 051602(R) (2013).
[42] V. V. Verbinski, H. Weber, and R. E. Sund, Prompt Gamma Rays from ^{235}U(n, f), ^{239}Pu(n, f), and Spontaneous Fission of ^{252}Cf, Phys. Rev. C **7**, 1173 (1973).
[43] S. J. Rose, F. Zeiser, J. N. Wilson, A. Oberstedt, S. Oberstedt, S. Siem, G. M. Tveten, L. A. Bernstein, D. L. Bleuel, J. A. Brown, L. Crespo Campo, F. Giacoppo, A. Görgen, M. Guttormsen, K. Hadyńska, A. Hafreager, T. W. Hagen, M. Klintefjord, T. A. Laplace, A. C. Larsen *et al.*, Energy dependence of the prompt γ-ray emission from the (d, p)-induced fission of ^{234}U* and ^{240}Pu*, Phys. Rev. C **96**, 014601 (2017).